HARDWARE DEVELOPMENT AND ERROR CHARACTERISATION FOR THE AFIT RAIL SAR SYSTEM

THESIS

Dayne A. Schmidt, Flight Lieutenant, RAAF

AFIT-ENG-MS-16-M-043

DEPARTMENT OF THE AIR FORCE
AIR UNIVERSITY

AIR FORCE INSTITUTE OF TECHNOLOGY

Wright-Patterson Air Force Base, Ohio

AFIT-ENG-MS-16-M-043

HARDWARE DEVELOPMENT AND ERROR CHARACTERISATION FOR THE AFIT RAIL SAR SYSTEM

THESIS

Presented to the Faculty

Department of Electrical and Computer Engineering

Graduate School of Engineering and Management

Air Force Institute of Technology

Air University

Air Education and Training Command

in Partial Fulfillment of the Requirements for the

Degree of Master of Science in Electrical Engineering

Dayne A. Schmidt, B.E. (Elec)

Flight Lieutenant, RAAF

March 2016

AFIT-ENG-MS-16-M-043

HARDWARE DEVELOPMENT AND ERROR CHARACTERISATION FOR THE AFIT RAIL SAR SYSTEM

THESIS

Dayne A. Schmidt, B.E. (Elec)
Flight Lieutenant, RAAF

Committee Membership:

Julie A. Jackson, PhD
Thesis Advisor

Richard K. Martin, PhD
Committee Member

Peter J. Collins
Committee Member

AFIT-ENG-MS-16-M-043

Abstract

This research is focussed on updating the Air Force Institute of Technology (AFIT) Radar Instrumentation Lab (RAIL) Synthetic Aperture Radar (SAR) experimental system. Firstly, this research assesses current hardware limitations and updates the system configuration and methodology to enable collections from a receiver in motion. Secondly, orthogonal frequency-division multiplexing (OFDM) signals are used to form (SAR) images in multiple experimental and simulation configurations. This research analyses, characterises and attempts compensation of relevant SAR image error sources, such as Doppler shift or motion measurement errors (MMEs). Error characterisation is conducted using theoretical, simulated and experimental methods. Final experimental results are presented to verify performance of the updated SAR collection system and show improvements to the final product through an updated methodology and various signal processing techniques.

Acknowledgements

I am grateful to the RAAF and AFIT for letting me experience this rare and unique opportunity. I would like to thank my AFIT colleagues for the many hours spent in RAIL discussing anything but radar and for the lunches spent treating ourselves. I must thank my parents from encouraging me from afar and bringing me several well-needed refills of Vegemite and Tim Tams to remind me of home. To my girlfriend: many thanks for I would not have been able to push through this task without all of your support, encouragement and motivation to keep going. Lastly, I must thank my advisor, Dr. Julie Jackson, for her guidance in many confusing situations and making sure this thesis came together in the end.

Dayne A. Schmidt

Table of Contents

Page

List of Figures

List of Tables

HARDWARE DEVELOPMENT AND ERROR CHARACTERISATION FOR THE AFIT RAIL SAR SYSTEM

I. Introduction

Given the abundance of ever-present radio frequency (RF) signals in the atmosphere, there is a high demand for passive bistatic radar (PBR) systems to exploit existing signals to determine information about the environment without requiring new transmitting platforms or fitting transmissions into the already dense RF spectrum. One particular area of PBR interest is synthetic aperture radar (SAR), which uses a moving receive antenna to collect RF signals and form an image of the environment. The goal of this research effort is to extend previous Air Force Institute of Technology (AFIT) work on bistatic synthetic aperture radar (BSAR) through updating the previous RF collection system to enable real-time experimentation, characterising sources of SAR image error and determining methods of error compensation to improve final SAR images.

Recent PBR research considers exploiting a large variety of communication signals in various applications. Such signals investigated include digital television [2,3,12–16], FM radio [17–19], cell phone communications [2–4, 20–24], or various other signal standards such as WiFi or WiMAX [5–7,25]. Digital communication signals vary significantly in frequency content and symbol structure, with some being mostly random in nature and others adhering to a strict set of international standards.

SAR systems often require sophisticated RF signals due to the fact that image resolution improves with higher signal frequency bandwidth, but a method for coherent phase detection is still required. One signal scheme commonly used in dig-

ital communications is orthogonal frequency division multiplexing (OFDM), which has both a consistent structure and adequate frequency components to be of use in advanced radar applications. Previous AFIT Radar Instrumentation Lab (RAIL) research [2–11] has shown that OFDM waveforms offer suitable complexity for successful SAR imaging whilst their prevalence in modern digital communications is ideal for passive BSAR development. Previous AFIT research has also established a baseline RF collection system for simple experimentation. One shortfall of the baseline AFIT system is that there only exists a method for move-stop-move collection, which is both tedious and time-consuming as well as an inaccurate reflection of possible real-world applications. This research will extend the baseline AFIT system to enable moving data collections in addition to refining previous methodology and user-system interfaces.

When considering a moving platform, or platforms, errors are introduced that can corrupt final SAR images [26–32]. These errors can be manifested through signal distortion or in signal processing errors. As the previous AFIT system [2–11] uses an averaged matched filter (AMF) for pulse detection and ranging, any signal distortion affecting the major signal characteristics, most prominently temporal Doppler shift, can affect AMF output and consequently reduce SAR image quality. Under large enough Doppler shifts, OFDM signals can suffer from inter-carrier interference (ICI) thus lowering signal-to-noise ratio (SNR) and causing incorrect detection [33]. This research will investigate the possible effects of Doppler shift in distorting SAR images and draw conclusions on the experimental impact for AFIT research.

In addition to possible signal distortion, system error can be manifested as incorrect assumptions regarding platform position or scene geometry. The previous AFIT system uses a backprojection algorithm (BPA) to project target returns onto a grid depicting the scene of interest and create a two-dimensional (2D) SAR image. Inac-

curate description of the pulse collection positions, or scene size geometry relative to those pulse collection positions, can result in errors in calculated target range during processing, thus forming a blurred SAR image [26, p.370-380], [27]. This research explores the effect of motion measurement errors (MMEs) on experimental SAR images and presents methods of compensation, including work done to extend and refine the previous AFIT SAR image production algorithms.

Chapter II of this thesis will outline the current state of the art in BSAR research using OFDM signals with particular focus on previous AFIT work and system limitations governing AFIT research. The relevant SAR background theory will also be outlined. Chapter III will detail the process used for updating the previous AFIT RAIL RF collection system through both hardware and software development. Preliminary experimental results will also be presented to prove that moving collections are achievable. Chapter IV will analyse possible sources of SAR imaging errors through theoretical development and realistic simulation. Error compensation methods will be proposed and final experimental results will be presented to show operation of the updated AFIT RAIL RF collection system. Chapter V will summarise the findings of this thesis and provide directions for future work. Through all chapters, it will be shown that this thesis makes the following contributions:

- Explores and outlines the limitations of current AFIT RAIL RF collection equipment.
- Updates previous methodology to enable moving receiver RF collections.
- Redesigns hardware configuration and software interface to streamline RF collection.
- Demonstrates ability for creating SAR images using moving collections.

- Characterises SAR image error sources and investigates actual impact in laboratory experimental setting.
- Creates robust simulations to realistically resemble real-world Doppler and MME effects.
- Proposes error compensation scheme and demonstrates its effectiveness through experimentation and SAR image creation.

II. Background

This chapter explores the current state of the art in passive BSAR with particular emphasis on previous AFIT research and other concepts related to this research. Whilst certain necessary PBR and SAR theory is introduced, it is assumed that the reader has a baseline knowledge of general radar and communications concepts, domain analysis, and signal processing techniques.

2.1 Previous AFIT Research

AFIT has previously led numerous research efforts into passive BSAR development [2–11]. These research efforts have focused on developing a simple RF collection system and determining the feasibility of passive BSAR using various OFDM communications signals. The focus of this thesis is to twofold; firstly, it will expand previous work to provide AFIT with a system capable of RF data capture from a receiver in motion and, secondly, it will form SAR images using the updated system, perform error characterisation and attempt error compensation for any image distortions.

2.1.1 Previous Major Contributions.

Forefront AFIT research [5–7, 9–11] evaluated the potential of using commercial OFDM signals for SAR imaging. Firstly, previous linear frequency modulation (LFM) deramping theory [34] was altered for both monostatic and bistatic OFDM signals through use of an AMF and inverse Fourier transform. Secondly, a bistatic BPA was implemented, and integrated with a total end-to-end simulation tool, software interface and RF collection system. Lastly, using arbitrary OFDM signals and benchmark WiMAX signals in the created experimental system, it was shown that passive BSAR was achievable.

Further AFIT research [2–4, 8] aimed to understand the full potential of passive BSAR using OFDM signals. Investigation was undertaken on Long Term Evolution (LTE), Digital Video Broadcasting-Terrestrial (DVB-T) and Digital Audio Broadcasting (DAB) signals through producing self ambiguity functions (SAFs) and cross ambiguity functions (CAFs) to understand signal properties, conducting link budget analysis for each signal on a passive BSAR scenario and via experimentation using the RF collection system described above. Additionally, a Matlab *passive radar toolbox* was created under the scope of [2] to refine previous signal processing and enable easier and more repeatable experimentation. The latest AFIT research [2–4, 8] found that, through signal ambiguity function (AF) analysis, a standardised signal structure enables the prediction of such things as peaks in the final SAR image outside an actual target, based upon the waveform used. Development on the experimental setup and Matlab toolbox resulted in a reliable baseline AFIT laboratory radar system, enabling future work.

To enable comparison with previous results, this thesis uses LTE, DVB-T and DAB signals as explored in [2–4, 8]. All signals are generated as per [2] with only the number of symbols varied to facilitate methodology changes. It is noted that the signals have been scaled to a centre frequency of $f_c = 2.5$ GHz and bandwidth of $B = 300$ MHz due to hardware limitations, but the structure of the signals remains consistent with the relevant standards [35–37]. Previous work [2] has shown that scaling the signal frequency content does not adversely affect experimental SAR image creation as the experimental scene size is also scaled down suitably.

2.1.2 Previous RF Collection System and Methodology.

The RF collection system used in all previous AFIT research [2–11] follows the diagram shown in Fig. 1, with different antennae dependent upon the scenario. The

AFIT RF collection system comprises a Matlab control graphical user interface (GUI), arbitrary waveform generator (AWG), stationary transmit antenna, receive antenna moving across a linear track and an oscilloscope to capture data for signal processing. The previous RF collection system was built around certain hardware limitations within the equipment available at AFIT.

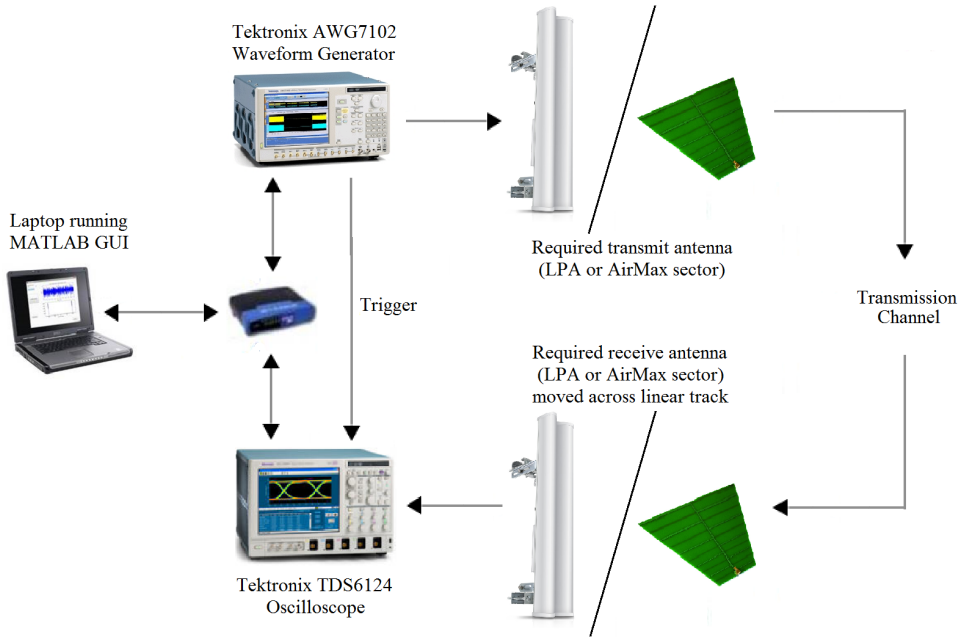

Figure 1. Basic AFIT RAIL experimental configuration.

2.1.2.1 Hardware Limitations and Previous Methodology.

Without procuring further hardware, the equipment shown in Fig. 1 provided certain hardware limitations that governed previous design choices and impacts the developments made in this thesis. The key hardware limitations come from the AirMax sector antennae used for signal transmit and receive, the track motor and laptop capabilities and the Tektronix TDS6124 oscilloscope used for data capture.

Firstly, the AirMax 2G-16-90 sector antenna was chosen due to its popularity in other WiMax RF systems and due to its large azimuth beamwidth compared to its

elevation beamwidth [9]. The AirMax sector antenna has a 6 dB azimuthal beamwidth of 90° and elevation beamwidth of 9° whilst the frequency coverage is $2.3 - 2.7$ GHz [38]. Whilst the AirMax antenna is designed to operate in the frequency bands that the LTE, DVB-T and DAB signals are designed and authorised to work at [35–37], a lack of large signal amplification is available through the Mini-Circuits® low-noise amplifiers owned by AFIT. Due to the low-transmission power available, close scenes and targets must be used in experimentation. The close proximity and arrangement of targets, in turn, has considerations when calculating imaging resolution, which will be discussed below. The AFIT RAIL also has various log periodic antennae (LPA) available to cover 0.4 – 6.5 GHz in different allocations, but this research uses the AirMax sector antennae due to their documented specifications and use in previous research [2–11].

Secondly, it is noted that the motorised track software allows a vast amount of freedom in receiver motion but the track's physical limitations restrict scenario variability. For example, stepped motion can be programmed to allow the receiver to travel at different speeds for different distances along the track, with different acceleration and deceleration times as well. A generic time-velocity profile of achievable receiver motion is shown in Fig. 2, where $v_{\mathrm{Rx},m}$ is the desired receiver velocity for segment m, t_{acc} is the receiver acceleration time, t_{dec} is the deceleration time and $t_{\mathrm{collection}}$ is the total time for the collection motion. In this research, the total time-velocity profile is defined as a piecewise function, $\psi(t)$, which will be used in Chapter IV for pulse position analysis. The starting velocity is a user-defined 'instantaneous' velocity for motion commencement and from which acceleration is based. The default starting velocity recommended by the manufacturer, and used throughout this research, is 0.001 m/s. Limits of operation for the AFIT track mean that the receiver is not capable of operating at speeds above $v_{\mathrm{Rx}} = 1$ m/s and only has a tested

hardware limit of $v_{\text{Rx}} = 0.6$ m/s with the receive antenna mounted. The acceleration and deceleration times can be programmed but there is a minimum of 0.5 seconds for the motor to reach operating speed, meaning that there will inherently be an acceleration and deceleration zone at each end of the track, even if programmed for constant velocity. Additionally, the physical track is 1.97 metres long, meaning RF pulses can only be collected within approximately ± 0.98 m from centre of the track. Due to the limited physical track length and desire to simplify experimental capture, this research will focus on implementing a single receiver velocity rather than the multi-segment example shown in Fig. 2.

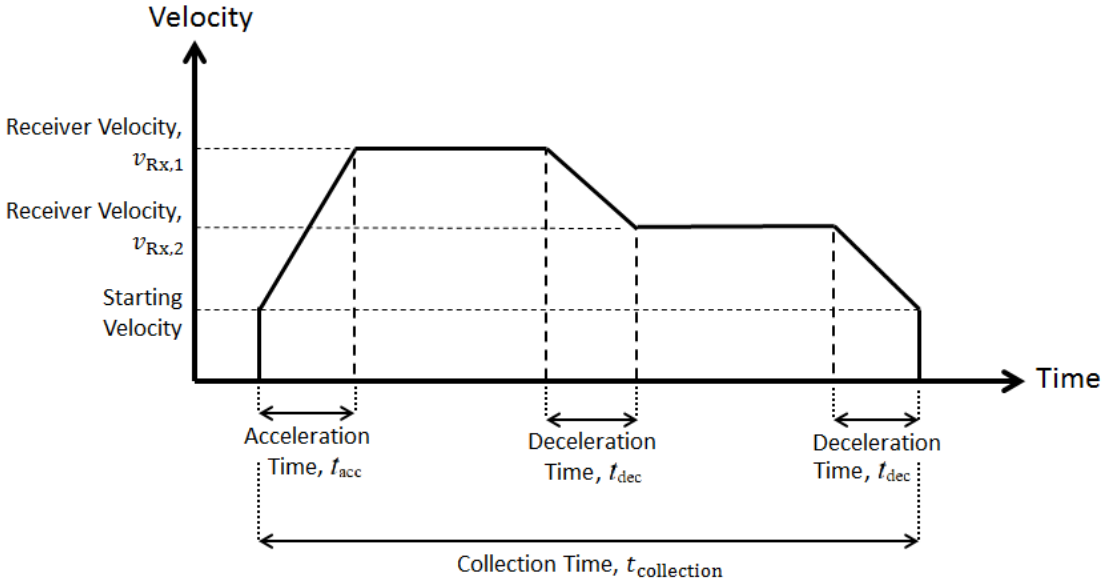

Figure 2. Motorised track generic scenario time-velocity profile, $\psi(t)$.

Thirdly, it is important to note the processing power of the laptop and Matlab version used in the AFIT RAIL RF collection system. The laptop is a Dell Latitude D630, running a 2.0 GHz processor and 2.0 GB of RAM. The laptop runs on Windows XP SP3 and all hardware interface is done through AFIT Matlab code, implemented in Matlab R2011b. Due to the antiquated hardware, processing times and data transfer capabilities limit certain functions of the software interface and will

be considered in Section 2.1.2.2 and Chapter IV.

Lastly, and most importantly, the previous RF collection methodology was predominantly built around hardware limitations in the form of acquisition memory size on the oscilloscope, or rather lack of ability to exploit all the features present on the Tektronix TDS6124C oscilloscope. The Tektronix TDS6124C oscilloscope with the 4M acquisition modification can sample at predefined, discrete rates up to and including 5, 10, 20 and 40 GS/s, with an acquisition memory of 64 MS per collection [39]. The baseline waveforms in [2–4, 8] were operated at a carrier frequency of $f_c = 2.5$ GHz and a bandwidth of $B = 300$ MHz, thus resulting in an upper frequency of 2.65 GHz and requiring the 10 GS/s acquisition mode to satisfy Nyquist sampling. The move-stop-move receiver measurement methodology was chosen since, for 10 GS/s acquisition rate, the 64 MS scope memory would fill in 6.4 ms. To traverse the 1.97 m linear rail in 6.4 ms, the receiver velocity required would be 307 m/s, which is physically unachievable due to hardware limitations. Thus, the receiver was stepped in a move-stop-move fashion, with each pulse saved individually to an external storage device and scope memory cleared between pulses. However, an unexplored feature of the oscilloscope, the Tektronix FastFrame$^{\text{TM}}$ segmented memory feature [39], can be used to enable multiple pulse captures without recording the 'off time' between pulses. The development of an updated methodology utilising the FastFrame$^{\text{TM}}$ feature will be explored in Chapter III, so this section will remain focused on previous methodology.

The previous move-stop-move methodology employs a single pulse being transmitted, reflected off targets and received at a fixed receiver position. The receiver is moved to the next stationary position on the linear track and the process is repeated. That is, each of P pulses is collected by a stationary receiver at predetermined track position, y_p, where P is the total number of azimuth pulse samples

and $p = \{0, 1, \ldots, P-1\}$ is the pulse number. Data must be stored after each pulse capture to prevent the oscilloscope memory from filling, so the total data collection takes on the order of hours (several minutes per pulse). After all P pulses are collected and saved in a move-stop-move fashion, the scene range profiles and phase history are computed using averaged matched filtering algorithms [5–7, 9–11] in Matlab. Additionally, a down-range calibration delay is applied to each result to account for system delays offsetting the origin of the range profiles at each azimuth step. Finally, a SAR image is produced using backprojection. The move-stop-move methodology caters to hardware limitations whilst still enabling a data capture across the azimuth extent with relative ease.

2.1.2.2 Previous Matlab Interface.

As described above, the previous move-stop-move methodology and equipment setup of Fig. 1 was refined across multiple research endeavours [2–11], including the development of a Matlab software interface to the RF collection system under the scope of [9]. A screenshot of the primary Matlab GUI windows previously used is shown in Fig. 3, where the red arrow indicates the progression of program windows.

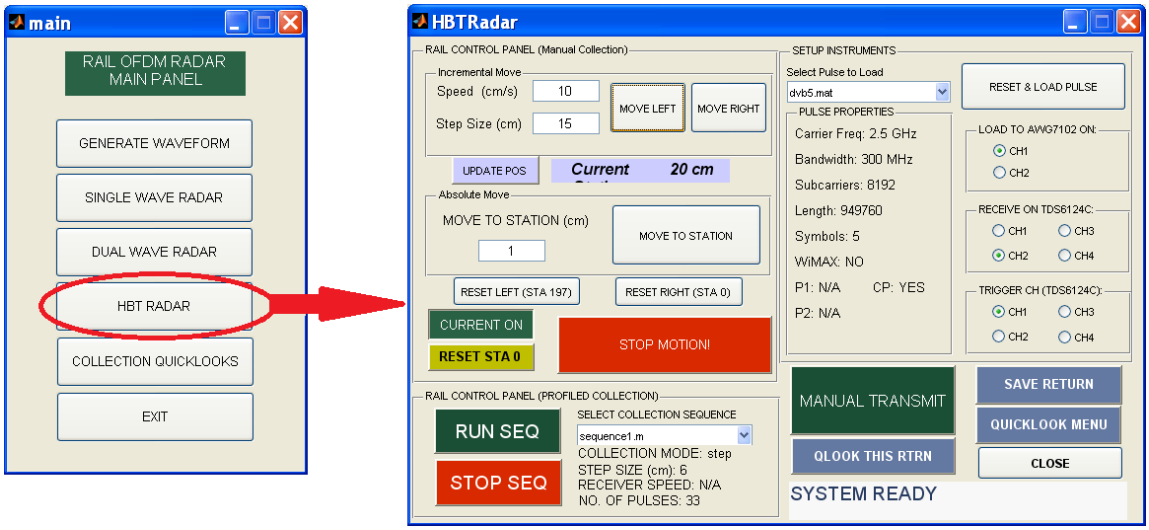

Figure 3. Previous Matlab GUI interface.

All functions of the Matlab GUI are accessed from the main screen and include the ability to generate waveforms for transmission, load signals on to one or both channels of the AWG, or use the 'HBT Radar' window shown in Fig. 3 to interact with the motorised track, oscilloscope and AWG to make a RF collection using one interface. The first key feature of the 'HBT Radar' interface shown in Fig. 3 is the ability to control the position and movement speed of the motor as well as controlling the current status and resetting the *zero station*, which is physically marked on the track and ensures future movements are accurate. The second key feature of the interface is the ability to load user-created waveforms onto the AWG and select trigger and reference channels for both the oscilloscope and AWG. The third key feature of the interface is the final step to either manually transmit a single pulse for collection, or run a collection sequence involving stepping the motor to predefined positions, y_n. It is noted that several aspects of the 'HBT Radar' interface, including the collection sequence, were not working within the legacy GUI. However, using the move-stop-move methodology, only the manual transmit function is required and the receiver is manually stepped between pulse locations so the inoperable features are not important.

Lastly, the "SAVE RETURN" button saves the single pulse collection from the oscilloscope to local disk. Due to the move-stop-move methodology, the process of saving a single pulse return can be achieved within data transfer limitations of the laptop. However, as the data size of the oscilloscope data increases substantially, the required increase in buffer size cannot be handled by the laptop processor, which will impact discussion on updating the software interface. Update and repair of the legacy Matlab GUI to suit an updated methodology will be detailed in Chapter III.

2.1.2.3 Signal Processing.

As mentioned, there is an AFIT *passive radar toolbox* for Matlab, created in [2], which enables easy and repeatable signal processing operations. The toolbox enables OFDM signals, including LTE, DVB-T and DAB, to be created following the relevant standards [35–37] and using desired values for features such as centre frequency, f_c, bandwidth, B, number of symbols, n_{sym}, and symbol length, T_{sym}. Operations are included to manipulate the time-domain OFDM signal by inserting certain data components (e.g. cyclic prefix, guard bands, reference symbols, direct current (DC) components, etc.) or by manipulating the signal format for frequency-domain analysis or for use with the legacy Matlab software interface described above. Predominantly however, the Matlab toolbox allows for a SAR image to be created using collected, or simulated, pulse reflection data in a specific format, along with scene geometry information. The key steps of the SAR image creation process using the AFIT passive radar toolbox are as follows.

1. *Populate phase history.* The first step in creating a spotlight SAR image is to collate all pulse collections into a phase history model. The phase history model contains complex return values for the signal at all operating frequencies within the bandwidth and across all collection azimuth positions. Phase history is obtained using a matched filter or deramp processing and is usually assumed to have both uniform frequency and temporal sampling for ease of processing [34]. As the phase of the return signal changes with the range at which it was reflected, the frequency values in the phase history model are related to differential range from scene centre through an inverse Fourier transform [2, 9, 34]. In the AFIT passive radar toolbox, the phase history is populated using an AMF process [2].

2. *Averaged matched filtering.* The phase delay of the signal is determined through implementation of an AMF, which coherently averages segments of each received pulse using an arbitrary segment length of the transmitted reference signal [2,9]. The coherent averaging across pulses distinguishes the AMF from a standard matched filter and is intended to reduce the effects of clutter and noise. The entire reference signal may be used, referred to as a 'full AMF', or only deterministic features may be used, referred to as a 'partial AMF'. It was previously shown [11] that the best results will be when the reference signal contains only those symbols expected to be present in the received signal for each particular AMF segment window. However, regarding LTE, DVB-T and DAB signals, Evers [2] showed that reliably accurate images are produced using a full AMF due to the assumption that the transmitted signal is known. Thus, this thesis will use the full AMF to produce results, with work being done to convert data from the new system into a format readily accessible using the previous passive radar toolbox.

3. *Generate SAR image.* Once created, the phase history data may be input to an image formation process such as polar reformatting, range migration or convolution backprojection (CBP) [2, 9, 34]. The BPA used in this research is filtered backprojection rather than CBP as it uses multiplication of a frequency ramp filter with the phase history data in the spatial frequency domain rather than convolution of the frequency ramp inverse Fourier transform (IFT) and the projection data in the time-domain. Each frequency multiplication result is summed to give integration across all synthetic aperture pulses and create a complete SAR image.

The focus of this current research effort is not to alter existing core functionality but rather extend hardware and software interfaces and accompanying signal pro-

cessing techniques to provide a more robust and capable experimental system for the AFIT RAIL. Further basic SAR theory will be briefly explored next to give context for the developments presented in this thesis.

2.2 Synthetic Aperture Radar Resolution

SAR imaging can be either *stripmap*, where a strip image is created from a single pass across a long scene, or *spotlight*, where a single focus point is imaged through using many collections from different look angles at the same scene. Typically, spotlight SAR provides higher resolution images, enables imaging of smaller scenes that are ideal for laboratory experimentation and can be used with both move-stop-move and continuous pulse collections [40]. Whilst this research employs a stripmap experimental setup, due to the linearly moving receiver with fixed look angle, data is processed using spotlight SAR imaging techniques. Spotlight and stripmap modes are geometrically interchangeable when the azimuthal extent is less than the total antenna beamwidth so that all pulse collections can be made without changing the flightpath or antenna look angle. The geometric interchangeability between spotlight and stripmap SAR also assumes a uniform beam pattern across the entire beamwidth, or some way to compensate for variations in antenna gain with azimuthal position. This research assumes the AirMax antennae have uniform gain across the entire beamwidth, as outlined in Section 2.1.2.1. Additionally, it will be shown in Chapters III and IV that the experimental configurations in this research contain all targets within the sector beamwidth of the AirMax antennae, thus justifying the use of spotlight signal processing techniques.

Two descriptive metrics of a monostatic spotlight SAR image are the down-range (ρ_x) and cross-range (ρ_y) resolution. The resolution values describe how finely any target reflections can be resolved within the final SAR image. Both resolution values

are measured as the distance from centre to first zero crossing of the target point spread responses and are given for an isotropic point scatter in the monostatic case as [34, Ch. 2]

$$\rho_x = \frac{c}{2B} \ , \tag{1}$$

$$\rho_y = \frac{\lambda}{2\Delta\phi} \ , \tag{2}$$

where c is the speed of light in m/s, B is the bandwidth of the signal in Hz, $\lambda = c/f_c$ is the wavelength of the signal in metres at the centre frequency of f_c Hz, and $\Delta\phi$ is the collection azimuth extent in radians, i.e., angular diversity of the flight path. When the radar is extended to a bistatic system, the resolution values vary by the line-of-sight (LOS) angles between the transmitter and the receiver. Specifically, the bistatic down-range and cross-range resolutions are [2], [26, Ch. 10]

$$\rho_x = \frac{c}{2B\cos(\beta/2)} \ , \tag{3}$$

$$\rho_y = \frac{\lambda}{4\sin(\Delta\phi/2)\cos(\bar{\theta}_b)\cos(\beta/2)} \ , \tag{4}$$

where β is the three-dimensional (3D) angle between the transmitter and receiver linse of sight and $\bar{\theta}_b$ is the bistatic LOS elevation angle for the centre pulse of the synthetic aperture, which is also the elevation angle of the phase-history support. Bistatic angle is typically measured from the centre of the synthetic aperture [34, Sect. 2.7], as shown in Fig. 4. For the case when the centre of the receive aperture aligns with the transmitter azimuth and the elevation difference between transmitter and receiver is near-zero, $\beta \approx 0$ and the geometry is known as *pseudomonostatic* [1]. For the pseudomonostatic case, the SAR image resolution is well approximated using the monostatic equations.

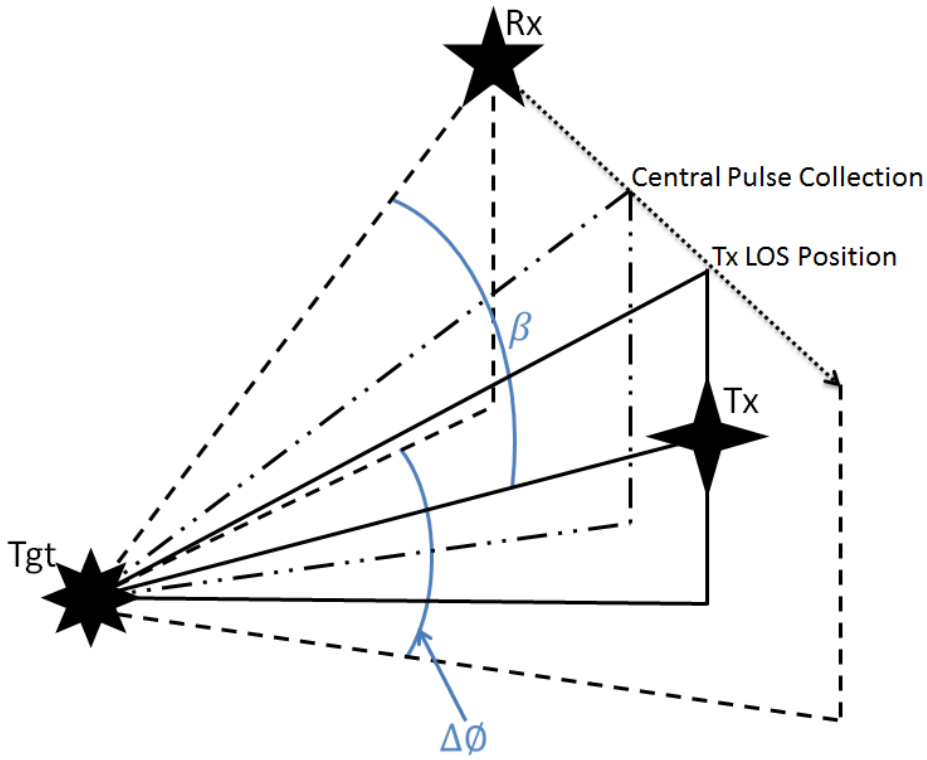

Figure 4. Bistatic radar system geomtery.

As shown in (1)–(4), signal bandwidth is a key factor affecting image resolution. In Section 2.1.2.1, low transmit power was stated as a reason for small experimental scenes. However, the best theoretical resolutions available for WiMAX, LTE, DVB-T and DAB signals are approximately 7.5 m [2, 9], meaning that targets would be indistinguishable in small experimental scenes. Thus, the operating frequency and bandwidth of the baseline signals have been scaled from $f_c < 0.75$ GHz to $f_c = 2.5$ GHz and $B < 50$ MHz to $B = 300$ MHz respectively [2]. Once experimental configurations have been established, expected image resolution for the scaled signals will be calculated using (3) and (4) and compared with actual obtained resolutions in Sections 3.2.2 and 4.3.

As described above, the previous AFIT RF collection system involves the collecting of a series of pulses across a synthetic aperture and signal processing using a Matlab passive radar toolbox to create a SAR image. In order to understand other possible

areas of impact on SAR image quality, outside of resolution decline, common areas of introduced error must be understood and investigated.

2.3 Error Sources in SAR Measurements

As with any application of radar, perfect detection and ranging is not possible due to real-world effects such as atmospheric distortion, temporal Doppler shifting, clutter, wavefront curvature and synchronisation issues. In SAR imaging, minor errors in target detection and ranging can propagate through phase-history creation and backprojection to create large image anomalies. This research will focus on analysing the errors due to AFIT's small scale laboratory setup, such as temporal Doppler shift, MMEs and wavefront curvature. A brief description of each error type follows.

2.3.1 Bistatic Doppler Shift.

2.3.1.1 Doppler Shift Calculation.

SAR image formation typically assumes that the pulse width is adequately small and that speed of light is much greater than platform speed, i.e, $c >> v_{\mathrm{Rx}}$, so that an echo pulse is collected by an effectively stationary platform—the so-called move-stop-move assumption [34]. The move-stop-move assumption greatly simplifies the matched filtering process in pulse collection, as no temporal Doppler shift needs to be accounted for. Previous AFIT research [2–11], by virtue of the hardware design discussed previously, has followed move-stop-move methodology by collecting each pulse at a stationary position before proceeding to the next collection point. Additionally, previous AFIT experimentation has used only stationary targets, thus nullifying any Doppler effects entirely.

However, for any real-life application, Doppler shift will be a necessary consid-

eration as platforms will be in motion during collection. Expanding upon the work of Willis [1, p. 119-129], the general bistatic Doppler shift for up to three moving platforms (transmitter, target and receiver) in the 2D plane can be calculated as

$$\begin{aligned} f_d &= \frac{1}{\lambda}\Bigg[v_{\mathrm{Tgt}}\cos\left(\delta_{\mathrm{Tgt}}-\frac{\beta_{\mathrm{2D}}}{2}\right)+v_{\mathrm{Tgt}}\cos\left(\delta_{\mathrm{Tgt}}+\frac{\beta_{\mathrm{2D}}}{2}\right) \\ &\qquad + v_{\mathrm{Tx}}\cos\left(\delta_{\mathrm{Tx}}-\phi_{\mathrm{Tx}}\right)+v_{\mathrm{Rx}}\cos\left(\delta_{\mathrm{Rx}}-\phi_{\mathrm{Rx}}\right)\Bigg], \\ &= \frac{1}{\lambda}\Bigg[2v_{\mathrm{Tgt}}\cos(\delta_{\mathrm{Tgt}})\cos(\beta_{\mathrm{2D}}/2)+v_{\mathrm{Tx}}\cos\left(\delta_{\mathrm{Tx}}-\phi_{\mathrm{Tx}}\right) \\ &\qquad + v_{\mathrm{Rx}}\cos\left(\delta_{\mathrm{Rx}}-\phi_{\mathrm{Rx}}\right)\Bigg], \end{aligned} \tag{5}$$

where λ is the operating frequency, $v_{\{\dots\}}$ are velocity vector magnitudes, $\delta_{\{\dots\}}$ are velocity angles, $\phi_{\{\dots\}}$ are azimuth look angles and $\beta_{\mathrm{2D}} = \phi_{\mathrm{Tx}} - \phi_{\mathrm{Rx}}$ is the 2D bistatic angle when transmitter and receiver elevation angles are approximately the same. Fig. 5 depicts the receiver (Rx), transmitter (Tx) and target (Tgt) geometry for (5). In Fig. 5, β_{2D} assumes that both transmitter and receiver are aimed directly at the target, as is the case in spotlight SAR. It is noted that the Doppler shift calculation of (5) assumes a 2D geometry where the transmitter and receiver are at zero altitude. Geometry knowledge is important for extending Willis' Doppler model as the $\cos(\cdot)$ terms are the projections of velocity vectors onto the respective LOS vectors [1]. This research approximates the total Doppler shift by using (5) with 3D angles. Each 3D angle is calculated using the dot product between the two relevant LOS vectors.

When Doppler shift is considered in signal processing techniques, a narrowband assumption is commonly used. The narrowband assumption implies that all frequency components of the signal are Doppler shifted by an equal amount across the entire bandwidth [41,42]. The narrowband assumption has repercussions for signal analysis in that if a single Doppler shift is considered for each pulse collection, that shift must be equal for signal components at the lower and upper ends of the bandwidth

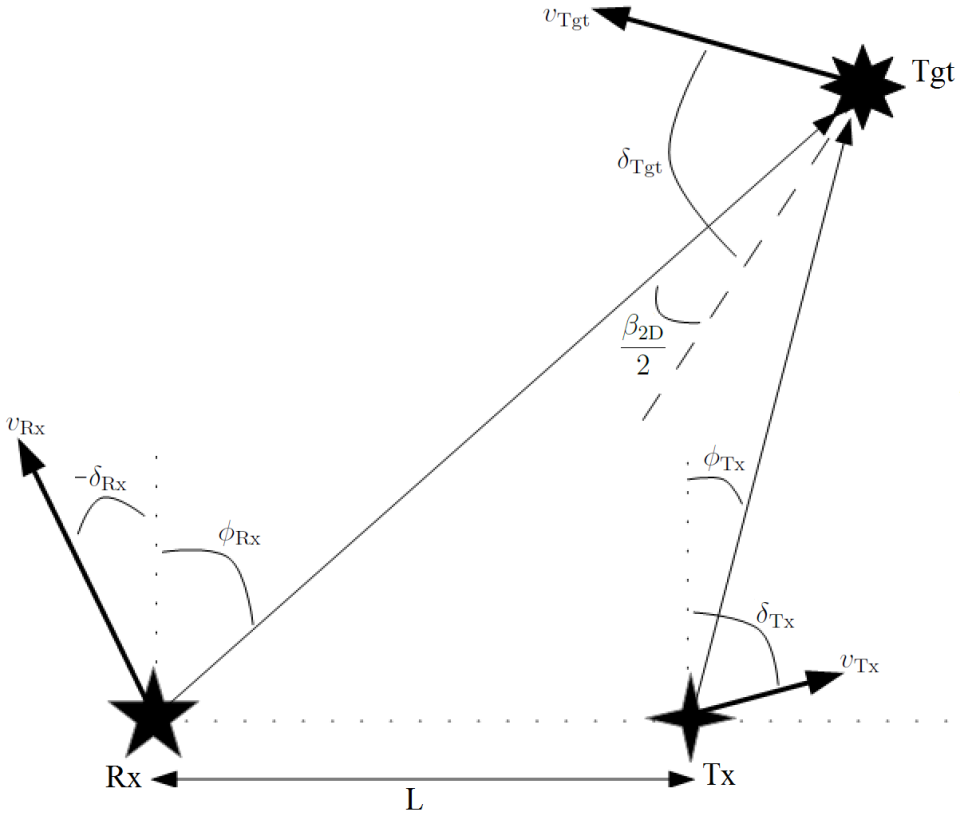

Figure 5. Bistatic Doppler geometry, based upon [1, p. 120].

as well as the centre frequency. Using Fig. 5 and (5), Doppler shift effects will be investigated in Chapter IV. Additionally, using the signals of interest, Doppler shifts will be investigated at bandwidth extremes to ensure validity of the narrowband assumption.

2.3.1.2 Modelling the Doppler Shift.

In order to understand where Doppler shifts can affect the SAR image construction process, the system is analysed as a whole. A flow chart indicating signal transmission is shown in Fig. 6, where $\mathrm{tx}(t)$ is the time-domain transmit signal, $g(t)$ is the scene reflectivity function and $\mathrm{rx}(t)$ is the time-domain receive signal. As this research focuses on the previous AFIT experimental model of a single moving receiver with a stationary transmitter and targets [2–11], it is assumed that a Doppler shift is

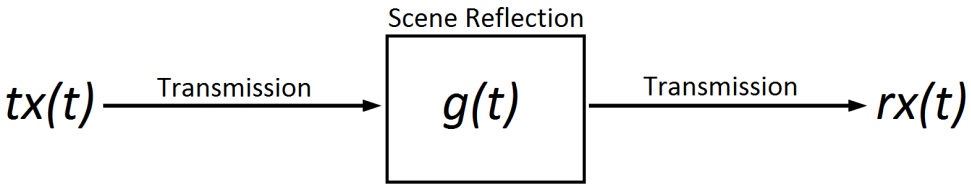

Figure 6. Radar system transmission flow chart.

only present at the receive platform, and is calculated using (5) with $v_{\mathrm{Tgt}} = v_{\mathrm{Tx}} = 0$ m/s. With the single receiver Doppler shift, f_d, the receive signal of Fig. 6 can be transformed to the frequency domain as

$$\mathrm{rx}(t) = \big(\mathrm{tx}(t) \star g(t)\big) e^{j2\pi f_d t} \ , \tag{6}$$

$$\mathrm{Rx}(f) = \mathrm{Tx}(f - f_d) G_{f+f_d}(f) \tag{7}$$

where $G_{f+f_d}(f)$ indicates the ideal scene reflectivity evaluated at frequency f, but stored at the shifted frequency, $f + f_d$, in the phase-history model. Calculating the scene reflectivity with the transmit frequencies but storing the response at the Doppler shifted receive frequency accurately reflects a scenario where only the receive platform is in motion, as is the case for this research.

For signal detection, the ideal matched filter output is expressed as $\mathrm{MF}(f) = \mathrm{Tx}^*(f)\,\mathrm{Rx}(f)$. Using the Doppler shifted receive signal of (7), the 'measured' matched filter output can be expressed as

$$\mathrm{MF}_m(f) = \mathrm{Tx}^*(f)\,\mathrm{Rx}(f) \ , \tag{8}$$

$$= \mathrm{Tx}^*(f)\,\mathrm{Tx}(f - f_d) G_{f+f_d}(f) \ . \tag{9}$$

Thus, separating (9) enables the measured matched filter output, $\mathrm{MF}_m(f)$, of a Doppler shifted signal to be modelled using three frequency-domain functions: the transmit signal complex conjugate, $\mathrm{Tx}^*(f)$, the Doppler shifted receive signal,

$\mathrm{Tx}(f-f_d)$, and the shifted ideal scene reflectivity, $G_{f+f_d}(f)$. Additionally, when there is zero Doppler shift, $f_d = 0$, and (9) reduces to $\mathrm{MF}_m(f) = \mathrm{Tx}^*(f)\,\mathrm{Tx}(f)G_f(f)$, as expected.

When considering an OFDM signal, the Doppler shift applies to all subcarriers under the narrowband assumption, as previously discussed. Each subcarrier, n, of the OFDM waveform carries modulated data, d_n, for a given symbol length, t_{sym}. Each symbol, ℓ, of the OFDM signal is equivalent to a rectangular function in the time-domain, or a sinc function in the frequency domain. As the total transmitted OFDM signal is the sum of all subcarriers across all symbols, the time-domain representation is

$$\mathrm{tx}(t) = \sum_{\ell=1}^{L}\left[\sum_{n=1}^{N}\left[d_{\ell,n}\cos(2\pi f_n t)\mathrm{rect}\left(\frac{t-(\ell-1)t_{\mathrm{sym}}}{t_{\mathrm{sym}}}\right)\right]\right] \ . \tag{10}$$

where f_n is the subcarrier frequency and $d_{\ell,n}$ denotes the modulated data for the ℓth symbol and nth subcarrier.

The Fourier transform of the rect function becomes a sinc function, meaning that the frequency-domain representation of the OFDM signal is a series of equal width sinc functions centred at the subcarrier frequencies, f_n, and of complex amplitudes, $d_{\ell,n}$. By taking a Fourier transform and ignoring negative frequencies, the OFDM signal is approximated by

$$\mathrm{Tx}(f) = e^{-j2\pi f(\ell-1)t_{\mathrm{sym}}}\sum_{\ell=1}^{L}\left[\sum_{n=1}^{N}\left[\frac{d_{\ell,n}}{2}\big(\delta(f-f_n)\star t_{\mathrm{sym}}\mathrm{sinc}(t_{\mathrm{sym}}f)\big)\right]\right] \ , \tag{11}$$

$$= \frac{e^{-j2\pi f(\ell-1)t_{\mathrm{sym}}}}{2}\sum_{\ell=1}^{L}\left[\sum_{n=1}^{N}\left[d_{\ell,n}t_{\mathrm{sym}}\mathrm{sinc}\big(t_{\mathrm{sym}}(f-f_n)\big)\right]\right] \ , \tag{12}$$

and when there is a Doppler shift introduced by the moving receiver, the shifted signal

component of (9) is

$$\mathrm{Tx}(f - f_d) = \frac{e^{-j2\pi f(\ell-1)t_{\mathrm{sym}}}}{2} \sum_{\ell=1}^{L} \left[\sum_{n=1}^{N} \left[d_{\ell,n} t_{\mathrm{sym}} \mathrm{sinc}\big(t_{\mathrm{sym}}(f - f_n - f_d)\big) \right] \right] \quad . \tag{13}$$

Equations (12) and (13) mathematically describe the OFDM Doppler shift phenomenom illustrated in Fig. 7. Using an arbitrary number of subcarriers and bandwidth, Fig. 7 shows how the subcarrier frequencies, f_n, are the shifted to the new frequencies of $f_n - f_d$. The Doppler shift in turn scales the output of the matched filter since the amplitude at the matched frequency is now $\tilde{d_n}$ instead of the original carrier amplitude, d_n, provided the received signal is sampled at the transmitted subcarrier frequencies, f_n. It is noted that all subcarriers may vary in amplitudes due to their different d_n terms, but they are shown at equal amplitude in Fig. 7 for simplicity of illustration.

The Doppler shift development described in this section – particularly (9), (12) and (13) – will be used in Chapter IV to develop a Doppler shift model of the experimental scenes under test and simulate the effects of Doppler shift on final SAR image production.

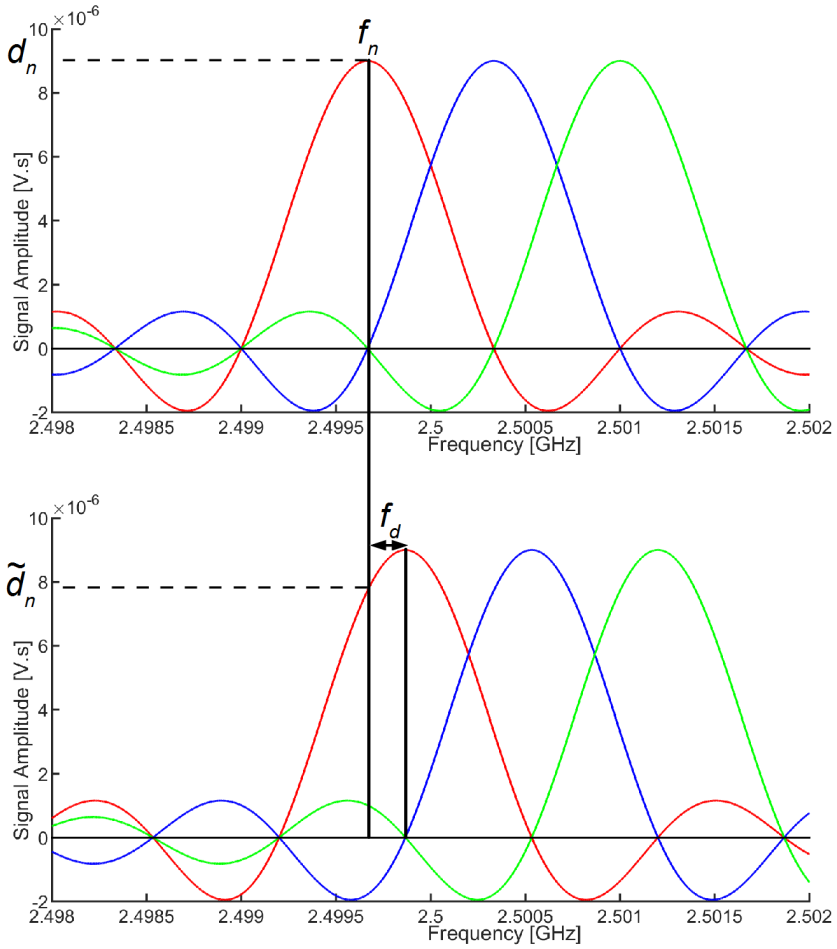

Figure 7. Doppler shift effect on OFDM signals.

2.3.2 Motion Measurement Errors.

As alluded to, SAR image formation algorithms depend upon accurate measurement of platform motion, thus allowing an accurate position and synchronisation between transmit and receive timing. MMEs result when the actual pulse collection position does not align with the pulse position used within the BPA. When there is discrepancy between the two position values, the differential range calculated during backprojection does not match with the echo range of the pulse, thus resulting in an inaccurate projection into the SAR image. When many pulses are misaligned, many 'targets' start to appear in the image, or if the projections are within resolution

cells of each other, a blurred image is created. As such, any position, velocity or acceleration MMEs can result in notable degradation of the final image.

MMEs can be characterised by an expression in the form of [26, p. 370-380], [27]

$$\tilde{\underline{r}}(\tau) = \tilde{\underline{g}}(\tau) + \tilde{\underline{h}}(\tau) \tag{14}$$

where τ is the pulse slow time vector, $\tilde{\underline{g}}(\tau)$ represents low-frequency errors and $\tilde{\underline{h}}(\tau)$ represents high-frequency errors. The high-frequency errors consist of noise-like interference, propagation and atmospheric effects and sinusoidal components with periods much shorter than the synthetic aperture duration [26, p. 370-380]. As high-frequency error components are hard to characterise and have limited effect in the laboratory environment, investigating low-frequency error components will be the focus of this research. Low-frequency error components consist of errors in measuring platform position, velocity and acceleration and can be modelled by a polynomial as [26, p. 370-380], [27]

$$\tilde{\underline{g}}(\tau) = \begin{bmatrix} \tilde{x}(\tau) \\ \tilde{y}(\tau) \\ \tilde{z}(\tau) \end{bmatrix} = \begin{bmatrix} \tilde{p}_x \\ \tilde{p}_y \\ \tilde{p}_z \end{bmatrix} + \begin{bmatrix} \tilde{v}_x \\ \tilde{v}_y \\ \tilde{v}_z \end{bmatrix} \tau + \begin{bmatrix} \tilde{a}_x \\ \tilde{a}_y \\ \tilde{a}_z \end{bmatrix} \frac{\tau^2}{2} \ , \tag{15}$$

where $[\tilde{p}_x \ \tilde{p}_y \ \tilde{p}_z]^T$ represents the error in measuring the platform's position at the synthetic aperture midpoint and $[\tilde{v}_x \ \tilde{v}_y \ \tilde{v}_z]^T$ and $[\tilde{a}_x \ \tilde{a}_y \ \tilde{a}_z]^T$ represent the error in measuring the platform velocity and acceleration respectively.

After establishing experimental methodology in Chapter III, MMEs will be revisited in Chapter IV for the scenes under test. The error vectors will be populated to render a low-frequency error vector, $\tilde{\underline{g}}$, specific to the experimental configuration and the resultant image distortions will be contrasted with actual experimental results.

2.3.3 Radar Wave Curvature.

During backprojection, it is usually assumed that all reflections lie on a straight line and can be easily interpolated to a Cartesian grid. However, due to the curved wavefront nature of RF waves as they radiate outwards, a scene that is larger than it is far away will cause targets at different cross-range positions to return larger down-range positions. However, as the scene distance becomes much larger than the scene diameter, the wavefront can be assumed to be a planar wave – commonly known as the far-field approximation – thus making geometric interpolation simpler.

In order to use the far-field approximation, two conditions must simultaneously be satisfied [40]:

1. The error in range due to wavefront curvature across the scene must be less than a resolution cell, as defined by (3) and (4). This condition ensures that any range errors do not push target returns into incorrect range cells.

2. The error in range due to wavefront curvature at any given point must vary by a small fraction of wavelength across all collection look angles. This condition ensures that targets are not blurred as different look angles give different ranges for use in the BPA.

Due to the large aperture width of SAR collections compared to the operating wavelength, near-field and far-field determination cannot be done by electromagnetic length, i.e., operating wavelength, but rather by diffraction behaviour. For SAR applications, the far-field approximation is considered valid for scenes that are at a distance greater than the Fresnel parameter [43],

$$S = \frac{D^2}{4\lambda}, \tag{16}$$

where D is the aperture length in metres, λ is the minimum operating wavelength

in metres and $S > 1$ m for a valid result. Using the Fresnel parameter, it will be shown in Sections 3.2.1 and 4.3 that the experimental scene configurations used in this research require near-field processing during backprojection.

III. Experimental Development and Preliminary Results

This chapter describes the process used in updating the AFIT RAIL RF collection system, including the reasoning behind design choices and solutions to certain hardware limitations. This chapter presents preliminary results showing the updated methodology in use and presents a way ahead for further experimentation in the remainder of this thesis.

3.1 RF Collection System Hardware

3.1.1 Real Time Collections.

In order to achieve a real-time capture spanning the entire track for P pulses at a given pulse repetition interval (PRI), the required receiver movement speed, v_{Rx} can be calculated as

$$v_{\text{Rx}} = \frac{D}{t_{\text{collection}}} \tag{17}$$

$$= \frac{D}{P \cdot \text{PRI} + t_{\text{echo}}} \tag{18}$$

where D is the traverse distance along the track or synthetic aperture length, $t_{\text{collection}}$ is the required collection time and t_{echo} is the roundtrip time for a pulse echo including travel time and pulse width. For experimental scenes considered with this hardware configuration, t_{echo} is less than 1μs due to the lack of transmit power available, restricting scene standoff distance. With such a small t_{echo}, the calculation of v_{Rx} becomes dominated by the P and PRI terms. Using an example signal pulse repetition frequency (PRF) of 200 Hz [9], or PRI = 5 ms, and the baseline [2–4, 8] $P = 33$ pulses and $D = 1.92$ m, $v_{\text{Rx}} \approx 11.6$ m/s $= 41.76$ km/hr is required for a collection spanning the entire track length. In order to lower v_{Rx} within the operating limits

outlined in Chapter II whilst maintaining maximum synthetic aperture length (D), either PRI or P can be increased, or a combination of both.

Increasing the signal PRI, i.e, reducing the PRF significantly, removes some real-world accuracy in the experimental model, since typical airborne SAR systems have a PRF of > 1 kHz [44, Table 2.1]. However, an accurate SAR image can still be created that is adequate for experimental investigation. For a given D and P, increasing the PRI will only lower v_{Rx} as per (18), consequently reducing possible Doppler effects on the received signal. However, increasing the PRI also dramatically increases the amount of unusable noise recorded during signal 'off time', assuming that a single continuous collection is used during the track traverse.

For example, choosing a realisable $v_{\text{Rx}} = 0.3$ m/s and maintaining $P = 33$ and $D = 1.92$ m gives a PRF ≈ 5.15 Hz, or PRI ≈ 193.9 ms, by rearranging (18). With a t_{echo} as defined above, there is a wasted receiver 'off time' of (PRI $- t_{\text{echo}}$) ≈ 193 ms. Ideally, P is increased and PRI is decreased to fill the 'off time' with more pulses and provide more data for analysis. Increasing P for a given cross-range travel extent will not increase the SAR image resolution, but it will increase maximum scene size before aliasing occurs.

However, the limitation in conducting a continuous collection is the acquisition memory of the oscilloscope. As described in Chap. II, the 64 MS scope memory will fill in 6.4 ms at a 10 GS/s sampling rate. Thus, regardless of the number of pulses within that interval, with $v_{\text{Rx}} = 0.3$ m/s and $D = 1.92$ m, the collection time spanning the entire track is $t_{\text{collection}} = 6.4$ s. This is much larger than the available oscilloscope continuous collection time, so a way to remove useless 'off time' data between pulses is presented next.

3.1.2 Oscilloscope Pulse Capture.

As alluded to in Chapter II, the Tektronix TDS6124C oscilloscope has the FastFrame$^{\text{TM}}$ feature [39], which can be utilised to overcome the oscilloscope acquisition memory filling too quickly in a moving collection. In FastFrame$^{\text{TM}}$ mode, the oscilloscope is triggered by the transmit pulse of the AWG to start capture for a fixed interval, the length of which is user defined according to the signal pulse width, T, and anticipated echo delay time, t_{echo}, for the scene of interest. At the end of the capture interval, the oscilloscope acquisition ceases until the transmit pulse triggers another acquisition one PRI later. FastFrame$^{\text{TM}}$ significantly reduces the amount of data by eliminating 'off time' between pulse echoes, thus enabling a longer total time period to elapse before the acquisition memory fills up.

Using the FastFrame$^{\text{TM}}$ feature, a series of pulse collections, known as frames[1], spanning the entire linear track can be made in one sweep. In order to cover the entire linear track in one sweep, the pulses must be spaced at sufficient intervals to allow the receiver to reach the next collection position, y_p, before receiving the next pulse. It is also desirable to have all received pulses evenly spaced across the entire aperture length so as to give maximum variation in data, thus allowing a better image construction. The PRI that facilitates such a collection with pulses evenly spaced across the entire track length is given by

$$\text{PRI} = \frac{t_{\text{collection}} - t_{\text{echo}}}{P} \tag{19}$$

$$\approx \frac{D}{v_{\text{Rx}} P} \tag{20}$$

[1]A FastFrame$^{\text{TM}}$ *frame* should not be confused with the *frame* of an OFDM signal. A FastFrame$^{\text{TM}}$ frame is a single capture of the data on the oscilloscope screen. A total SAR collection consists of P frames, each with the reflected pulse data included within. An OFDM frame, however, consists of all encoded data as outlined by the relevant signal standards, including all reference bits, cyclic prefixes and data symbols [45].

where $t_{\text{collection}}$ is the required collection time, t_{echo} is the roundtrip time for a pulse echo including travel time and pulse width, P is the number of pulses for collection, D is the traverse distance along the track and v_{Rx} is the desired receiver speed.

Due to the laboratory nature of the experimental configurations considered in this research, the standoff distance to the scene is small enough that $t_{\text{echo}} << t_{\text{collection}}$ and the calculation of PRI becomes dominated by the P and $t_{\text{collection}} = D/v_{\text{Rx}}$ terms, as per (20). For example, using $v_{\text{Rx}} = 0.3$ m/s and $P = 33$ pulses, as previously introduced, a PRI ≈ 193.9 ms can be used to capture a single collection across the entire track. Transmitting the signal at a given PRI is achieved by loading the signal into the Tektronix AWG7102 AWG and setting it to run in triggered mode with an internal trigger equal to the PRI.

Fig. 8 shows a timing diagram depicting the pulse and collection timings for a single frame. Transmit pulse p is sent at time t_p, triggering the FastFrame$^{\text{TM}}$ acquisition for the specified interval equal to $t_{\text{collection}}/P$. The echo pulse is received after t_{echo} and fully recorded within the capture window, assuming an appropriate time interval is chosen. The oscilloscope then ceases acquisition until triggered again by transmit pulse $p + 1$. It is noted that the FastFrame$^{\text{TM}}$ recording technique is most suitable for experimental configurations where $t_{\text{echo}} << T$, so that the recording window is dominated by the receive pulse after being triggered by the transmit pulse. This is the case for our research where $t_{\text{echo}} < 1\mu$s and $T \approx 100$–200μs.

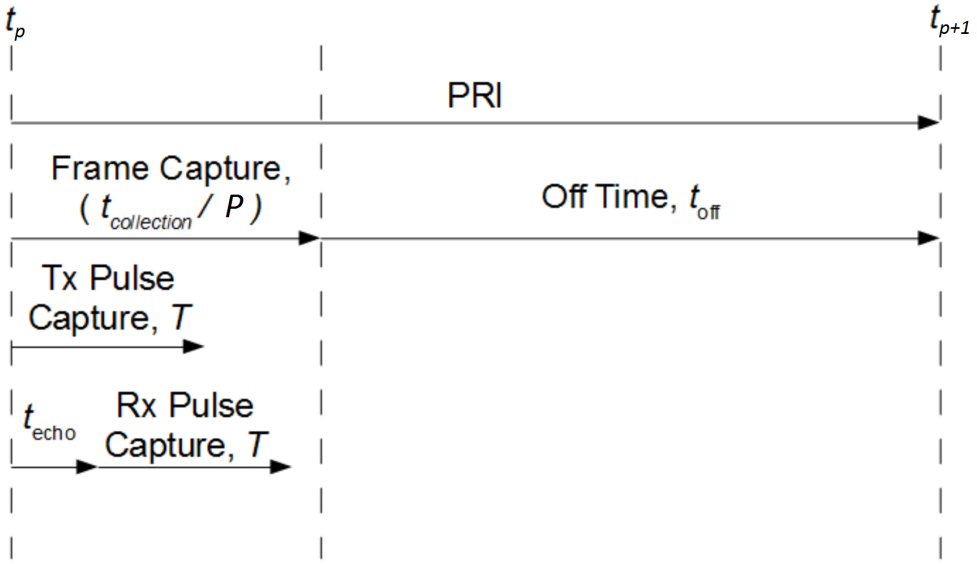

Figure 8. Bistatic RF collection system timing diagram using FastFrame™ pulse collection.

3.1.3 Experimental Tradeoffs.

The experimental configurations in this research use $D = 1.92$ m and $v_{\text{Rx}} \in \{0.1, 0.2, 0.3, 0.4, 0.5\}$ m/s with all signals operated at $f_c = 2.5$ GHz and $B = 300$ MHz. The baseline configuration of [2–11] uses $P = 33$ and pulse widths of $T \lessapprox 200\mu$s. Unfortunately, to use identical OFDM signals and capture all pulses using FastFrame™, the oscilloscope would require an acquisition memory of at least $n_{\text{samp}} = f_{\text{samp}} NT = 10$ GHz $\times 33$ pulses $\times 200\mu$s $= 66$ MS per channel. Additionally, by using the transmit channel to trigger the frame collections, twice the acquisition memory is required, thus increasing the total collection length to 132 MS for a full collection using 33 pulses. Without modifying the system for improved capture ability, the $n_{\text{samp}} = 64$ MS acquisition memory limitation can be facilitated by lowering any combination of the P, T, f_{samp} or the number of recorded channels, n_{channels}, in

$$n_{\text{samp}} = n_{\text{channels}} PT f_{\text{samp}} \ . \tag{21}$$

Using Nyquist sampling for the baseline OFDM signals [2–11] requires a sampling frequency of $f_{\text{samp}} = 10$ GS/s, so this is kept constant throughout this thesis. However, using (21), T, P and n_{channels} are varied one at a time through the following three design choices:

1. *Pulse number reduction.* In order to balance pulse collection capability with sampling fidelity using FastFrame$^{\text{TM}}$, P is reduced from 33 to 16 pulses. With $P = 16$, the oscilloscope can record 16 frames of 4 MS each.

    - The length of 4 MS corresponds to a 10 GS/s sampling rate for 200 μs on two channels (transmit trigger and receive signals), thus satisfying Nyquist sampling criteria for frequencies up to 5 GHz and pulse widths, T, up to 200 μs. It is noted that actual DAB, LTE and DVB-T symbol and OFDM frame lengths are significantly in excess of 200μs [2, Table 2.2], but that the scaled baseline signals lower these to ensure total pulse widths of $T \lessapprox 200\mu$s [2, Table 5.1].
    - Choosing $P = 16$ does not affect the final image resolution provided that the cross-range extent is not reduced. However, scene aliasing can occur if there are not enough samples across the rail aperture extent. For scene radius, r_{scene}, and minimum operating wavelength, λ_{min}, the sample spacing must satisfy $\delta\phi \lessapprox \frac{\lambda_{\text{min}}}{4r_{\text{scene}}}$. For $r_{\text{scene}} = 3$ m and $\lambda_{\text{min}} = c/f_{\text{max}} = c/(f_c{+}B/2) = 0.1131$ m, the maximum sample spacing, $\delta\phi_{\text{max}} = 0.0094$ radians $= 0.5402$ degrees. The azimuthal sample spacing is calculated as $\delta\phi = \tan^{-1}(D/(PR_R))$, where R_R is the receiver range to scene centre. For a collection of 16 pulses spanning the 1.92 m track at a distance of 13 m to scene centre, samples are spaced at 0.12 m along the track, or at $\delta\phi = 0.5289$ degree azimuthal steps. As $\delta\phi < \delta\phi_{\text{max}}$, the pulse spacing satisfies the requirement to avoid scene aliasing.

- The naming convention used here indicates the signal type along with the corresponding number of symbols used to give the longest pulse whilst maintaining $T \lessapprox 200$ μs. The three signals tested under this configuration are a DAB signal with 23 symbols (DAB23), a DVB-T signal with 5 symbols (DVB5) and an LTE signal with 23 symbols (LTE23). Parameters for these signals are listed in Table 1 and results using these signals will be presented in both Chapters III and IV.

2. *Pulse width reduction.* In order to fit a number of pulse collections close to the baseline of $P = 33$ within acquisition memory, the signal pulse widths are reduced to below 100μs by adjusting the number of transmit symbols. With $T \lessapprox 100\mu$s, the $P = 32$ is used since the oscilloscope can record 32 frames of 2 MS each.

   - The length of 2 MS corresponds to a 10 GS/s sampling rate for 100 μs on two channels (transmit trigger and receive signals), thus satisfying Nyquist sampling criteria for frequencies up to 5 GHz and pulse widths, T, up to 100 μs, which are both required for adequately capturing the shortened DAB, LTE and DVB-T signals.

   - Due to the pulse compression of OFDM signals, scene resolution is only a function of signal frequency and bandwidth and collection azimuthal extent and bistatic angle. Thus, lowering the pulse width of the signal does not affect scene resolution, or affect scene aliasing as the same number of samples are acquired across the same azimuth extent. However, lowering the pulse width does in turn lower the SNR of the AMF output, as the coherent integration time is reduced [2].

   - The shortened pulse width is achieved by lowering the number of symbols

in the OFDM communication signals to satisfy $T = n_{sym}T_{sym} < 100\mu$s, where T is the total pulse width, n_{sym} is the number of communication symbols and T_{sym} is the length of each communication symbol, without changing any other structural components of the signal.

- The three signals tested under this configuration are a DAB signal with 11 symbols (DAB11), a DVB-T signal with 2 symbols (DVB2) and an LTE signal with 11 symbols (LTE11). Parameters for these signals are listed in Table 1 and results for these signals will be presented in Chapter IV.

3. *Transmit Signal Removal.* In order to maximise receive signal collection within the acquisition memory, one can record only the receive channel. Thus, using the baseline signal pulse widths of $T \lessapprox 200\mu$s, the oscilloscope can record 32 frames of 4 MS each.

   - The length of 4 MS corresponds to a 10 GS/s sampling rate for 200 μs on one channel (receive signal), thus satisfying Nyquist sampling criteria for frequencies up to 5 GHz and pulse widths, T, up to 200 μs, which are both required for adequately capturing the baseline DAB, LTE and DVB-T signals.

   - By removing the transmit pulse, the 64 MS acquisition memory can be filled by only the receive signal, thus allowing capture of $P = 32$ baseline receive pulses. However, without the transmit signal for accurate triggering, the FastFrame$^{\text{TM}}$ feature relies upon the power of the receive signal to trigger frame capture.

   - With the absence of a transmit signal to trigger frame collection, it is found that some receive pulses are dropped through the oscilloscope triggering on noise to capture a frame. As such, this configuration is unreliable and

dropped in favour of the two proceeding configuration options, where either reduced length pulses or a reduced number of pulses is used, but not both.

Table 1. Parameters of signals used for experimental testing, based upon baseline signals from [2–4, 8].

Parameter	**Symbol**	**LTE11**	**LTE23**	**DVB2**	**DVB5**	**DAB11**	**DAB23**
Operating mode	-	FDD		8k		TxI	
Carrier frequency (GHz)	f_c	2.5					
Data symbol duration (μs)	T_u	6.8		27.3		6.8	
CP Ratio	Δ_g	1/4		1/4		63/256	
Symbol duration (μs)	T_{sym}	8.5		34.1		8.5	
Subcarrier separation (kHz)	Δf	146.5		36.6		146.5	
Data subcarriers	N_a	1320		6816		1536	
Subcarriers per symbol	N	2048		8192		2048	
Effective bandwidth (MHz)	B_{eff}	193.51		249.65		225.15	
Bandwidth (MHz)	B	300					
Symbols	N_{sym}	11	23	2	5	11	23
Signal duration (μs)	T	93.9	196.3	68.3	170.7	93.9	196
Modulation scheme	-	DQPSK		64QAM		64QAM	

Following collection using the selected pulse configuration, the sampled data is manually downloaded from the oscilloscope for signal processing and image creation. The single FastFrame$^{\text{TM}}$ data file contains all receive pulses from each collection, so the save operation need only be performed once, significantly speeding up the overall data collection time compared to the move-stop-move collections in [2–11]. The P pulse returns are separated and average matched filtered [7, 9, 11]. Finally, a down-range calibration delay is applied to each range profile, as in the move-stop-move collection, prior to SAR image formation. The improved data collection method enables measurement of both stationary and moving targets from a receiver in motion. However, Doppler effects and image defocus may result from receiver, target or transmitter platform motion, as discussed in Chapter II and analysed in Chapter IV.

3.2 Preliminary Experimental Collection

Using the updated hardware configuration and FastFrame^{TM} feature implementation described above, preliminary experimental results were obtained to test the basic functionality and promise of results using the updated methodology.

3.2.1 Outdoor Experimental Configuration.

Using the basic AFIT RAIL hardware configuration of Fig. 1 the scene configuration shown in Fig. 9 was constructed outdoors. This scene is used as a known working model to compare new techniques to previous AFIT work [2–4, 8]. As established in Section 3.1, this outdoor scene experimental configuration uses $D = 1.92$ m, $v_{\text{Rx}} \in \{0.1, 0.2, 0.3, 0.4, 0.5\}$ m/s and contains four 0.6×0.6 m metal plate targets.

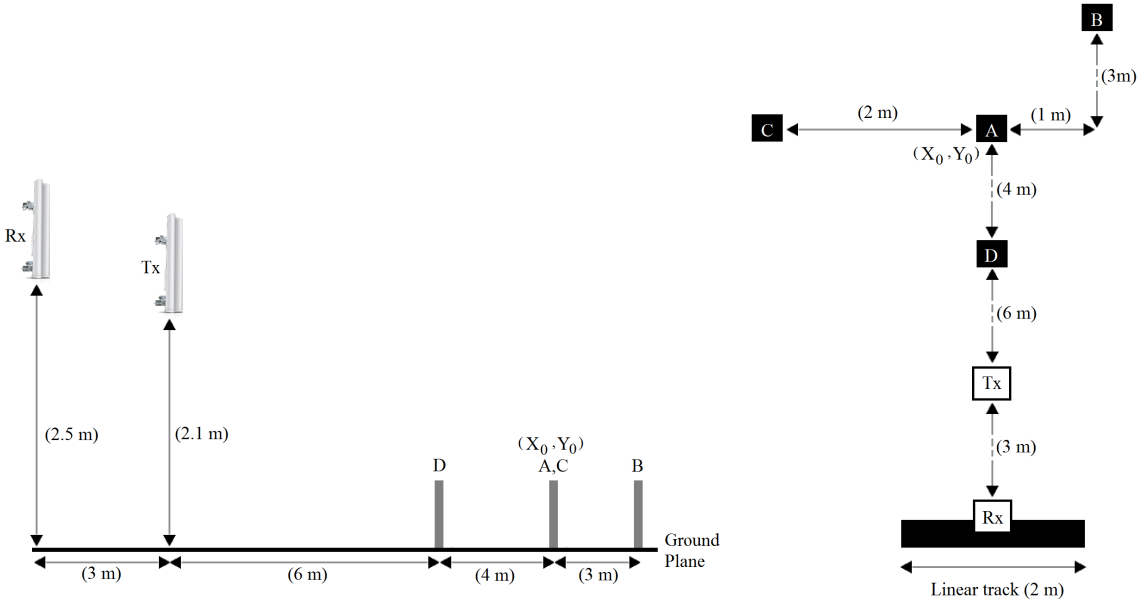

(a) Side view. (b) Top view.

Figure 9. Outdoor scene setup based upon previous AFIT experimentation [2–11]. All targets are 0.6×0.6 m metal plate targets.

In order to expedite preliminary results, initial testing using the FastFrame^{TM} feature used the same hardware configuration shown in Fig. 1, but with a rudimentary

software interface instead of the updated RAIL Matlab GUI yet to be developed in Section 3.3. Initial testing was conducted by loading a single pulse of the signal under test into the Tektronix AWG7102 arbitrary waveform generator. The pulse was exported from Matlab as a single text file containing real sample values at a sampling rate of $f_{\text{samp,Tx}} = 5.565$ GHz. The FastFrame$^{\text{TM}}$ settings were chosen as per the rationale presented in Section 3.1 such that all pulses fell within the range of the oscilloscope display (obtained with a range of 10.0 μs/div) and had a sampling rate of $f_{\text{samp}} = 10$ GS/s as that is lowest sampling rate available on the oscilloscope that satisfies Nyquist sampling. For receiver motion, the legacy motor GUI was used to set start and stop locations of 0.04 and 1.96 m respectively (thus giving $D = 1.92$ m) and choose a desired v_{Rx}.

With the transmitter constantly illuminating the scene, a collection was completed by the user simultaneously triggering the receiver to start motion and the oscilloscope to start capture of the FastFrame$^{\text{TM}}$ pulses. In order to obtain pulses evenly spread across the entire track length, the AWG7102 was set to run in trigger mode with an internal trigger interval calculated using (20). The data file was manually downloaded from the oscilloscope for signal processing and image creation. However, in order to use existing AFIT image generation algorithms, the single FastFrame$^{\text{TM}}$ data file from each collection had to be separated by pulse return in order to be processed at the given pulse collection locations. Finally, each pulse collection was used with an AMF to create the phase-history and a BPA was used to create resultant 2D images.

As discussed in Chapter II, the scene must lie outside the distance dictated by (16) in order to be assumed at the far-field. Using an aperture diameter of $D = 1.92$ m and a minimum operating frequency of $\lambda = (3 \times 10^8)/(2.35 \times 10^9) = 0.1277$ m, a Fresnel parameter of $S \approx 7.22$ metres is obtained. Although most targets within the scene of Fig. 9 are outside a distance of 7.22 metres, target D is within the Fresnel

distance of the transmitter. Thus, near-field processing is used for creating images of the outdoor experimental scene of Fig. 9.

In this outdoor experimental configuration, the centre of the receiver aperture is at the same azimuthal position as the transmitter, meaning there is zero azimuthal bistatic angle, and the 3D bistatic angle reduces to the elevation bistatic angle, $\bar{\theta}_b$. For the experimental configuration of Fig. 9, the elevation bistatic angle is

$$\bar{\theta}_b = \cos^{-1}\left(\frac{(\overrightarrow{\mathrm{Tx}} \cdot \overrightarrow{\mathrm{Rx}})}{\left|\overrightarrow{\mathrm{Tx}}\right|\left|\overrightarrow{\mathrm{Rx}}\right|}\right) , \tag{22}$$

$$\approx 0.0170 \text{ radians} , \tag{23}$$

where $\overrightarrow{\mathrm{Tx}}$ and $\overrightarrow{\mathrm{Rx}}$ are the transmitter and receiver LOS vectors from scene centre respectively. Thus, using $B = 300$ MHz, $\lambda = c/f_c \approx 0.1199$ m and a receiver range of $R_R = 13$ m to scene centre from Fig. 9, the azimuth extent is calculated as

$$\Delta\phi = 2\tan^{-1}\left(\frac{0.5\ D}{R_R}\right) , \tag{24}$$

$$= 2\tan^{-1}\left(\frac{0.96}{13}\right) \approx 0.1474 \text{ radians}, \tag{25}$$

and the expected resolution values can be approximated using (3) and (4) as

$$\rho_x = \frac{c}{2B\cos(\beta/2)} = 0.4997 \text{ m, and} \tag{26}$$

$$\rho_y = \frac{\lambda}{4\sin(\Delta\phi/2)\cos(\bar{\theta}_b)\cos(\beta/2)} = 0.4071 \text{ m}. \tag{27}$$

For the reasons outlined in Section 3.1.3, two collections were made; one with shortened signals and one with the full-length baseline LTE, DVB-T and DAB signals, as developed in [2–4, 8]. In both cases, the receiver was run at speeds of $v_{\mathrm{Rx}} \in \{0.1, 0.2, 0.3, 0.4\}$ m/s and also $v_{\mathrm{Rx}} = 0.5$ m/s for full-length signals. The parameters

for all signals used are listed in Table 1, where the naming convention combines signal type and number of symbols, e.g., 'LTE23' is an LTE signal with 23 symbols.

3.2.2 Outdoor Experimental Results.

3.2.2.1 Half-length Signal Collection.

Using LTE11, DVB2 and DAB11 signals, as described in Table 1 at $v_{\text{Rx}} \in \{0.1, 0.2, 0.3, 0.4\}$ m/s, selected resultant SAR images are shown in Figs. 10 – 12. Using near-field processing during the BPA results in the curved isorange contours clearly visible at each of the target ranges in Figs. 10 – 12. In all figures, targets A, B and D are clearly visible at their respective range ellipse and centred at their actual location within the scene.

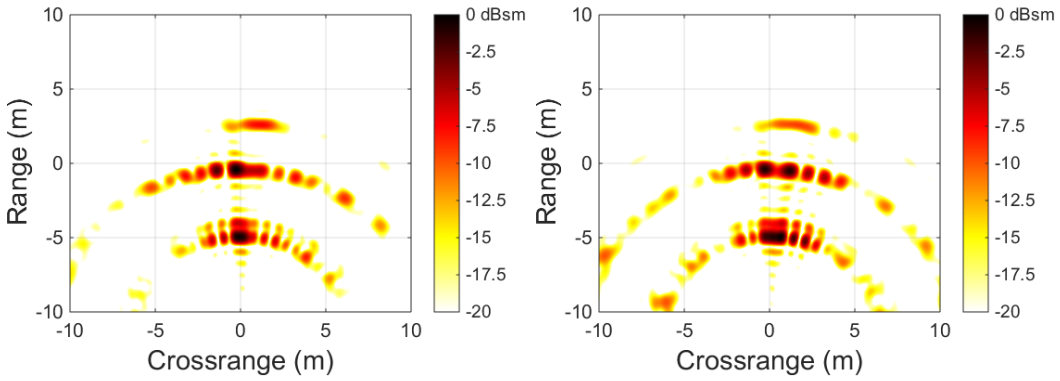

(a) $P = 32$; $v_{\text{Rx}} = 0.1$ m/s (b) $P = 32$; $v_{\text{Rx}} = 0.4$ m/s

Figure 10. Comparison of bistatic SAR images formed using the DAB11 signal and different receiver collection speeds.

However, with targets A and C having actual ranges of 13 and 13.153 m from the aperture centre respectively, they appear along the same isorange contour since the range difference between the two is less than the down-range resolution of $\rho_x =$ 0.4997 m, as calculated in Section 3.2.1. Conversely, since the cross-range resolution of $\rho_y = 0.4067$ m, as calculated in Section 3.2.1, is less than the separation of targets A and C, a small separation is visible between the two targets. To confirm the

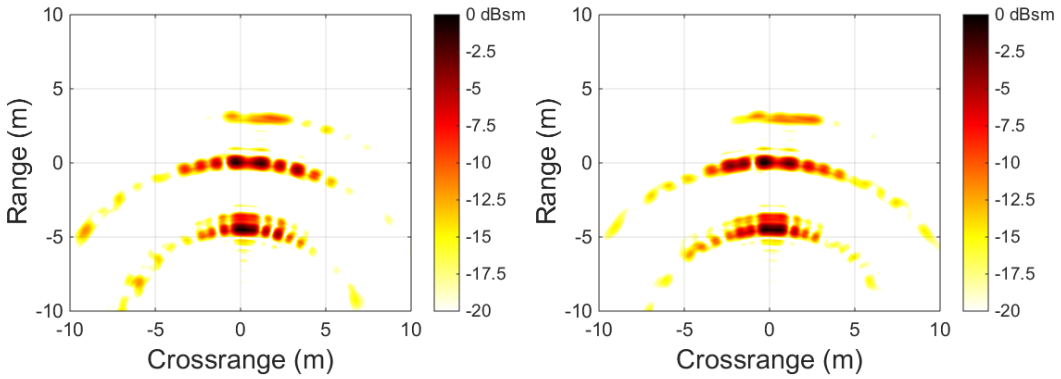

(a) $P = 32$; $v_{\mathrm{Rx}} = 0.1$ m/s (b) $P = 32$; $v_{\mathrm{Rx}} = 0.4$ m/s

Figure 11. Comparison of bistatic SAR images formed using the DVB2 signal and different receiver collection speeds.

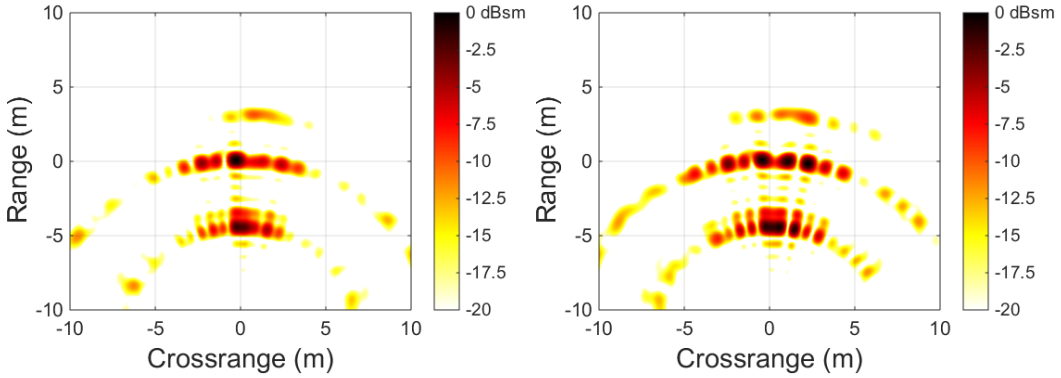

(a) $P = 32$; $v_{\mathrm{Rx}} = 0.1$ m/s (b) $P = 32$; $v_{\mathrm{Rx}} = 0.4$ m/s

Figure 12. Comparison of bistatic SAR images formed using the LTE11 signal and different receiver collection speeds.

resolutions of the image, the image is zoomed in on an individual target return and an estimated resolution cell is manually placed around the target response's first null, as shown in Fig. 13. The resolutions are measured as half of the cell height and width. Using the example shown in Fig. 13, the down-range resolution is measured as $\rho_x \approx 0.70$ m and the cross-range resolution as $\rho_y \approx 0.70$ m. The best possible theoretical results of $\rho_x = 0.4997$ m and $\rho_y = 0.4071$ m have not been reached in this experimental configuration due to significant image blurring and distortion. Sources of image distortion will be investigated in Chapter IV.

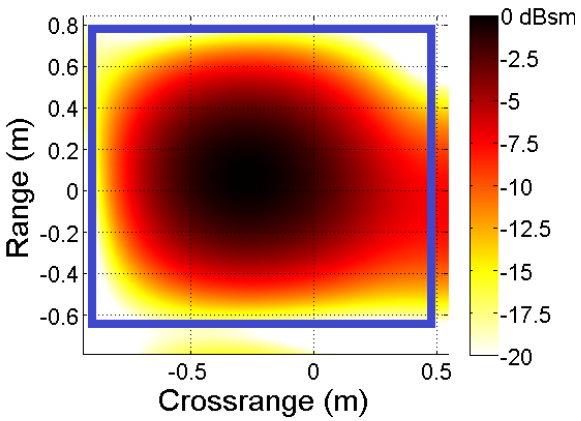

Figure 13. SAR image resolution measurement using the LTE11 image of Fig. 12(a). Down-range and cross-range resolutions measured as $\rho_x \approx 0.70$ m and $\rho_y \approx 0.70$ m respectively from centre of target.

It is also noted that each image contains returns that do not align with any actual target within the scene. As discussed in Chapter II, the most probable causes of these anomalies are Doppler shift or MMEs. Error analysis is conducted throughout further system development in Chapter IV; however the preliminary results indicate that SAR images can indeed be formed using the updated moving RF collection methodology.

3.2.2.2 Full-length Signal Collection.

Increasing the signal length from the results presented above to $T \lessapprox 200\mu$s and decreasing the pulse number to $P = 16$, as per the rationale presented in Section 3.1.3, collections were taken using the baseline DAB23, DVB5 and LTE23 signals from Table 1. These collections were taken both using the move-stop-move method of [2–11] and at $v_{\text{Rx}} \in \{0.1, 0.2, 0.3, 0.4, 0.5\}$ m/s. Selected resultant SAR images are shown in Figs. 14 – 16, with Figs. 14(a), 15(a) and 16(a) showing results from previous experimentation [3] for comparison.

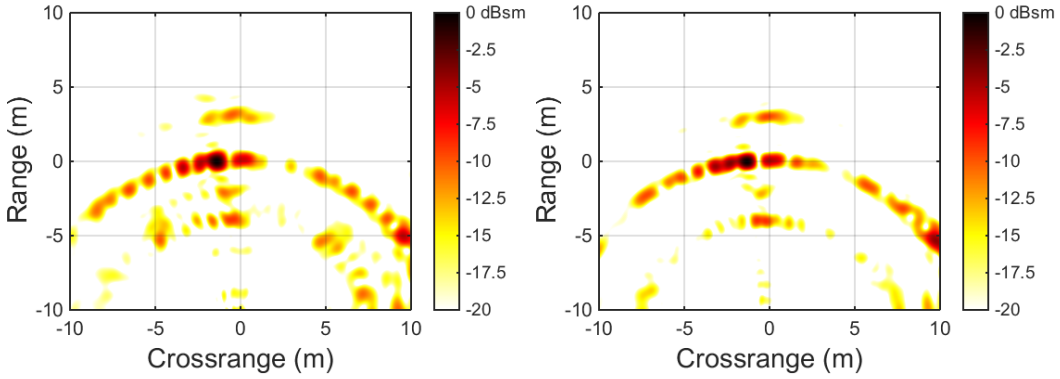

(a) $P = 33$; move-stop-move (used with permission from [3])

(b) $P = 16$; move-stop-move

(c) $P = 16$; $v_{\mathrm{Rx}} = 0.1$ m/s

(d) $P = 16$; $v_{\mathrm{Rx}} = 0.5$ m/s

Figure 14. Comparison of bistatic SAR images formed using the DAB23 signal and different receiver collection speeds.

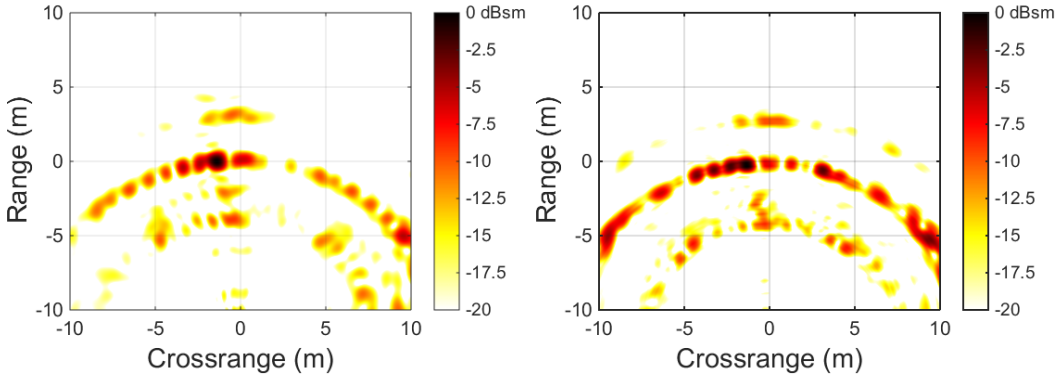

(a) $P = 33$; move-stop-move (used with permission from [3])

(b) $P = 16$; move-stop-move

(c) $P = 16$; $v_{\mathrm{Rx}} = 0.1$ m/s

(d) $P = 16$; $v_{\mathrm{Rx}} = 0.5$ m/s

Figure 15. Comparison of bistatic SAR images formed using the DVB5 signal and different receiver collection speeds.

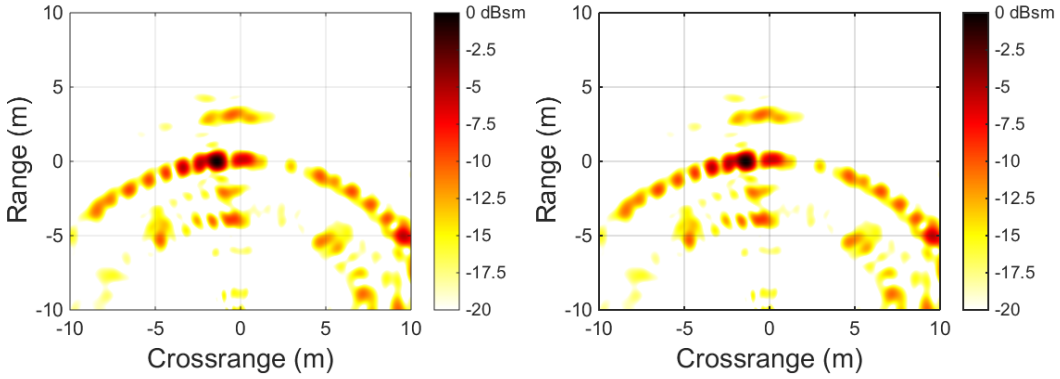

(a) $P = 33$; move-stop-move (used with permission from [3])

(b) $P = 16$; move-stop-move

(c) $P = 16$; $v_{\mathrm{Rx}} = 0.1$ m/s

(d) $P = 16$; $v_{\mathrm{Rx}} = 0.5$ m/s

Figure 16. Comparison of bistatic SAR images formed using the LTE23 signal and different receiver collection speeds.

As in the preceding half-length signal results, Figs. 14 – 16 are constructed using near-field processing resulting in curved isorange contours. Despite the number of pulses dropping to $P = 16$, neither the signal bandwidth, operating frequency, azimuthal extent or bistatic angles have changed so the theoretical down and cross-range resolutions remain at $\rho_x = 0.4997$ m and $\rho_y = 0.4071$ m respectively, as calculated in Section 3.2.1. Again, the actual image resolution is measured zooming in on an individual target return and estimating a resolution cell around the target response's first null. Using the example shown in Fig. 13, the down-range resolution is measured as $\rho_x \approx 0.80$ m and the cross-range resolution as $\rho_y \approx 0.75$ m. Again, significant blurring and image distortion has resulted in resolution degradation, and this will be investigated in the next chapter.

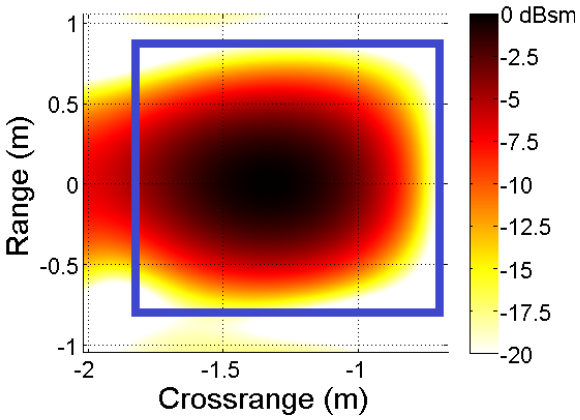

Figure 17. SAR image resolution measurement using the LTE23 image of Fig. 16(c). Down-range and cross-range resolutions measured as $\rho_x \approx 0.80$ m and $\rho_y \approx 0.75$ m respectively from centre of target.

Whilst large numbers of anomalies are still visible in Figs. 14 – 16, intensity of the target returns is generally higher than the resultant images using half-length signals presented in Figs. 10 – 12. This can be partially attributed to the higher SNR from a larger coherent processing time in the AMF when using the longer signals. However, partial cause for target intensity differences between any two given images is due to susceptibility of the outdoor scene to minute configuration changes. For example,

the four metal plate targets used must be aligned individually during experimental set up to ensure an adequate reflection between the transmitter and receiver LOS. The aspect of the closest target (D) must also be adjusted to lower its radar cross section (RCS) so that returns from the farthest target do not drop below the dynamic range during the normalisation process. This configuration fragility greatly affects the repeatability of any experiments on this outdoor scene, with results possibly varying between signal sets simply through the wind and atmospheric effects. The half-length signal results of Figs. 10 – 12 were taken on a different day than the full-length signal results of Figs. 14 – 16, as were the previous results of Figs. 14(a), 15(a) and 16(a), and the RCS amplitude of target D was different on all three occasions.

A luxury afforded in the move-stop-move method is the ability to choose which pulses are saved for each azimuthal location. By being selective and only saving 'good' pulse returns, a higher energy output is possibly obtained from the matched filter. Whilst this has limited effect on image quality, it does mean the main beam lobes of each target can be at a higher level, as seen via comparison between Fig. 14(b) and Fig. 14(c) for example. However, as seen in Figs. 14(b), 15(b) and 16(b), the move-stop-move technique of [2,3] is not completely reliable for repeatable and distortionless SAR image production. Additional blurring in the SAR images produced via move-stop-move methodology can be attributed to pulse anomalies as well as unaccountable equipment effects such as antenna vibration from the wind or system noise. In particular, during data collection for this experimental setup, strong intermittent wind gusts were present, thus shaking both antennae and toppling the transmitter multiple times. Due to the variability in experimental setup, as well as lowering the amount of data available by using $P = 16$ pulses, a reliable comparison between the previous results of Figs. 14(a), 15(a) and 16(a) with the new move-stop-move results of Figs. 14(b), 15(b) and 16(b) is difficult to make.

3.3 Software Interface Development

The Matlab GUI previously created [9] is designed for move-stop-move stationary pulse capture and does not integrate with FastFrame^{TM} or continuous transmission of a signal to enable a collection spanning the entire track. In order to conduct more robust testing using the extended hardware methodology presented in Section 3.1, an updated Matlab GUI is presented here. The software interface is not only updated to automate and simplify experimentation but also attempts to reduce the synchronisation errors found in the preliminary experimentation of Section 3.2.

The updated GUI contains all legacy features as described in [9] and Chapter II, but also provides a new interface, as shown in Fig. 18, for running moving collections using the FastFrame^{TM} feature and continuous signal transmission.

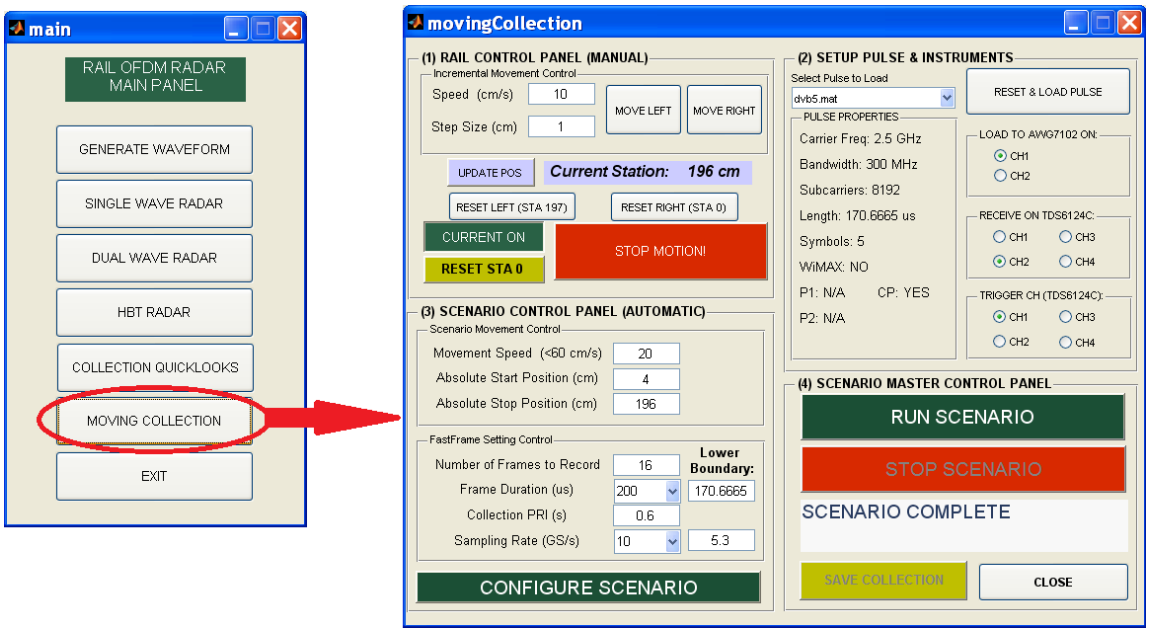

Figure 18. Updated Matlab GUI continuous collection interface.

The GUI is firstly accessed by from the main menu by selecting the "MOVING COLLECTION" button, as shown in Fig. 18. The moving collection window allows users to incrementally move the receiver (noting that the *zero station* must be accu-

rately set at the start of operation), select a transmit signal (s_{Tx}), configure collection parameters and run the scenario. For scenario configuration, the user is able to enter a movement speed (v_{Rx}), start and stop positions, a number of frames (P) to record and select a frame duration ($t_{\mathrm{collection}}P$) and sampling rate (f_{samp}) from the list of available oscilloscope options. When the user selects a pulse and presses "RESET & LOAD PULSE", the desired pulse and selected channel settings are loaded to the AWG and oscilloscope, and the *lower boundary* fields for scenario configuration are populated. The lower boundaries are used to ensure that the selected frame duration is long enough to capture the pulse data and that the selected sampling frequency is high enough to satisfy Nyquist criterion. When the "CONFIGURE SCENARIO" button is pressed, error checking is carried out to ensure, amongst other criteria, that the oscilloscope acquisition memory is adequate for the desired settings. The PRI is populated using (20) with the values entered by the user, and all the appropriate settings are loaded onto the oscilloscope and AWG so that the system is ready.

Collection is started using the "RUN SCENARIO" button on the interface in Fig. 18, which triggers the AWG to start transmission, the oscilloscope to start capture and the receiver rail motor to start motion and recording position data. The system then waits until movement has finished before shutting off transmission and alerting the user to save the receive channel pulse data manually from the oscilloscope. The "STOP SCENARIO" and "SAVE COLLECTION" buttons in Fig. 18 have been disabled in this release of the GUI as motor motion cannot be stopped whilst 'waiting' is underway and collection saving cannot be automated due to the laptop hardware limitations mentioned in Chapter II restricting the buffer size available to Matlab.

When the user saves the receive pulses following collection, the oscilloscope produces a single file of P pulses concatenated as double values. Using a different Matlab script, the single FastFrame$^{\mathrm{TM}}$ data file from each collection is separated into pulse

returns before the phase history and a SAR image are produced through matched filtering and a BPA. Additionally, a down-range calibration delay is applied to each result to account for system delays offsetting the origin of the range profiles at each azimuth step. This delay term is applied as a phase shift in the spatial frequency domain, translating to a spatial shift after an inverse Fourier transform, and was tailored to align the image of target A to $(0, 0)$. It was found that the delay term varies with the signal construct, but stays consistent across receiver velocities for any given signal. For example, the DAB signals include zero-padding prior to encoded data whilst the LTE and DVB-T signals do not. The zero-padding is transmitted from the AWG but is discarded during the oscilloscope triggering process so that the DAB signal has an effectively longer transmission time.

3.4 Chapter Conclusion

This chapter has detailed the rationale and process used in updating the AFIT RAIL RF collection system to enable moving data collection. It was shown that the Tektronix FastFrame^{TM} feature is capable of capturing pulses across the entire motorised track, or synthetic aperture length, and that SAR images can be created. It was seen that four targets were visible in an outdoor experimental scene, but that image quality varied between signal type used and experimental conditions. Lastly, an updated Matlab GUI was presented to automate and simplify further experimentation. Error analysis and indoor experimentation using the updated software interface will next be presented to show maturity of the RF collection system after removing outdoor environmental and human input factors.

IV. Error Analysis and Further Results

This chapter discusses and analyses various sources of error within SAR images previously shown. Error characterisation is conducted and an error compensation method is proposed, with further experimental testing conducted using the RF collection system updates presented in Sections 3.1 and 3.3 on an indoor scene.

4.1 Doppler Shift Error Analysis

4.1.1 Mathematical Determination.

In updating experimental methodology to enable moving RF collections, it is desirable to see what effect, if any, Doppler may have upon SAR image formation and the validity of assuming move-stop-move for an actual moving platform. For the experimental setup in Fig. 9, $v_{\text{Tgt}} = v_{\text{Tx}} = 0$, so the bistatic Doppler shift of (5) reduces to

$$f_d = (1/\lambda)\left[v_{\text{Rx}} \cos\left(\delta_{\text{Rx}} - \theta_{\text{Rx}}\right)\right] , \tag{28}$$

where angle $\theta_{\text{Rx}} \in [-4.22^\circ, 4.22^\circ]$ and angle $\delta_{\text{Rx}} = -90^\circ$ (for $D = 1.92$ m centred at $y = 0$). Then, for receiver velocities of $v_{\text{Rx}} \in \{0.1, 0.2, 0.3, 0.4, 0.5\}$ m/s and operating frequencies in $[f_{min} = 2.35, f_{max} = 2.65]$ GHz, the predicted Doppler shifts are listed in Table 2. The maximum absolute Doppler shift present is approximately 0.33 Hz (when $v_{\text{Rx}} = 0.5$ m/s) and the maximum discrepancy between the frequency extremes of the bandwidth is less than 0.05 Hz (at $v_{\text{Rx}} = 0.5$ m/s). The negligible difference between Doppler shifts at each end of the signal bandwidth validates the narrowband assumption that Doppler shift is equal across all subcarriers of the OFDM signal. Additionally, as the $\delta_{\text{Rx}} - \theta_{\text{Rx}}$ term of (28) is independent of the bistatic angle, all

Doppler shifts will be equal to the values listed in Table 2 when the centre of the receiver linear track is at boresight to the target, as per the experimental setup of Fig. 9.

Table 2. Bistatic Doppler shift calculation for various receiver positions in the outdoor scene configuration of Fig. 9.

v_{Rx} (m/s)	Rx Start Pos		Rx Mid Pos		Rx End Pos	
	@f_{min}	@f_{max}	@f_{min}	@f_{max}	@f_{min}	@f_{max}
0.1	0.0577 Hz	0.0651 Hz	0 Hz	0 Hz	-0.0651 Hz	-0.0577 Hz
0.2	0.1155 Hz	0.1302 Hz	0 Hz	0 Hz	-0.1302 Hz	-0.1155 Hz
0.3	0.1732 Hz	0.1953 Hz	0 Hz	0 Hz	-0.1953 Hz	-0.1732 Hz
0.4	0.2309 Hz	0.2604 Hz	0 Hz	0 Hz	-0.2604 Hz	-0.2309 Hz
0.5	0.2886 Hz	0.3255 Hz	0 Hz	0 Hz	-0.3255 Hz	-0.2886 Hz

4.1.2 Simulation of Doppler Influence.

With such small temporal Doppler shifts presented in Table 2, it is expected that there will be limited to no effect on the final SAR image unless look angles and/or platform velocities are increased significantly. However, in order to validate this prediction, a realistic Doppler shift simulation is developed.

4.1.2.1 Simulation Design.

In order to demonstrate the effects of Doppler shift on SAR image creation, simulations are created in Matlab using the following process:

1. Create Cartesian coordinate system defining a scene of desired dimensions. As introduced in Chapter II, the convention is used which defines down-range as x, cross-range as y, with all units in metres and referenced to scene centre.

2. Insert receiver(s) and transmitter(s) in scene at desired coordinates with desired motion properties.

3. Insert target shapes in scene at desired locations and angular aspect. An example scene containing four rectangular plates is shown in Fig. 19, which aligns to the experimental scene setup of Fig. 9.

4. Convert all Cartesian coordinates to spherical (azimuth and elevation). Again, as introduced in Chapter II, the convention is used where azimuth is defined as starting from the positive x-axis toward the negative y-axis.

5. Calculate Doppler shift for each azimuth position of receiver motion, as outlined in Section 2.3.1.2.

6. Calculate total scene phase-history at the receiver as a sum over individual phase histories for all target returns. Only direct target reflections are considered in phase-history construction with no multi-path simulation conducted. As described in Section 2.3.1.2, the phase-history model is altered to simulate Doppler shift by:

   (a) Calculating the scene reflectivity at the transmit frequencies and storing it at the Doppler shifted frequencies $G_{f+f_d}(f)$. Target contributions to the phase-history models are calculated using bistatic scattering models for 3D shapes developed in [46].

   (b) Applying a complex amplitude scaling factor of $\mathrm{Tx}^*(f)\,\mathrm{Tx}(f - f_d)$, as derived in (9).

7. Use the BPA to create a SAR image from each receiver's scene phase history. The implementation of the BPA varies with whether the scene is in the radar near-field or far-field as discussed in Chapter II and dictated by (16).

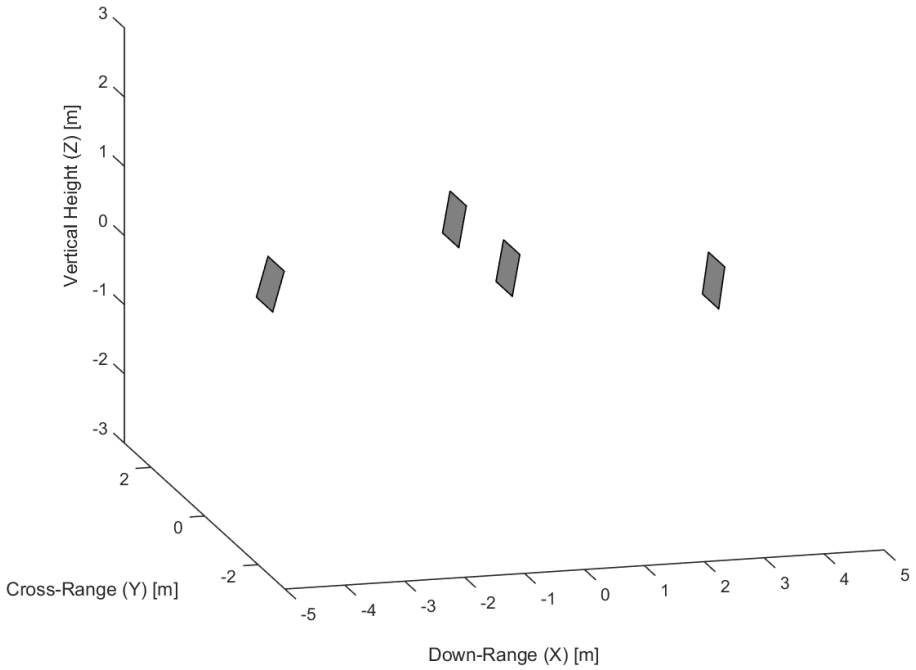

Figure 19. Basic AFIT RAIL experimental scene configuration from Fig. 9, as simulated in Matlab.

4.1.2.2 Simulation Results.

Using the simulated scene of Fig. 19, with an DAB23 signal and $v_{\mathrm{Rx}} = 0.5$ m/s, SAR images[2] are generated in Fig. 20. It can be seen that, between the zero Doppler image of Fig. 20(a) and the theoretical Doppler image of Fig. 20(b), there is no noticeable difference between the target definition in the two SAR images, thus suggesting that the Doppler values in Table 2 are small enough to not significantly affect the final image. Observing the difference image of Fig. 20(c), shows that introducing the Doppler shifts of Table 2 does indeed have an effect on the final image, but that the differences are at significantly low magnitudes (observe the altered dBsm scale). The introduction of the theoretical Doppler has had negligible effect in the main scene

[2]The direction of isorange contour curvature in the simulation images is different to that of experimental results. This is due to an assumed sign difference in differential range processing during backprojection. This convention difference has no effect on the location of central target responses so it has been ignored during this research.

focus area around the targets, but it can be seen in the upper and lower areas that there is down-range 'ringing' due to the minor frequency errors introduced by the Doppler. It is important to note that Doppler can affect images easily, but observing the minimal simulated impact on SAR images for the outdoor scene, Doppler will be dismissed as an area of significant error.

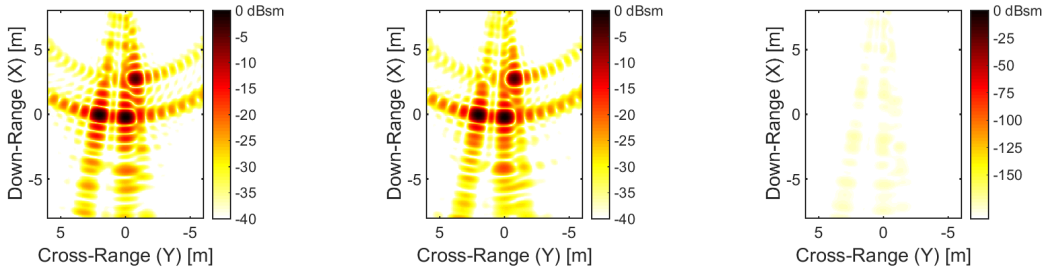

(a) Zero Doppler shift introduced.

(b) Theoretical Doppler shifts of Table 2 introduced.

(c) Difference image of (a) and (b).

Figure 20. SAR images created of the simulated scene in Fig. 19 to investigate the effects of introducing the theoretical Doppler shift values of Table 2.

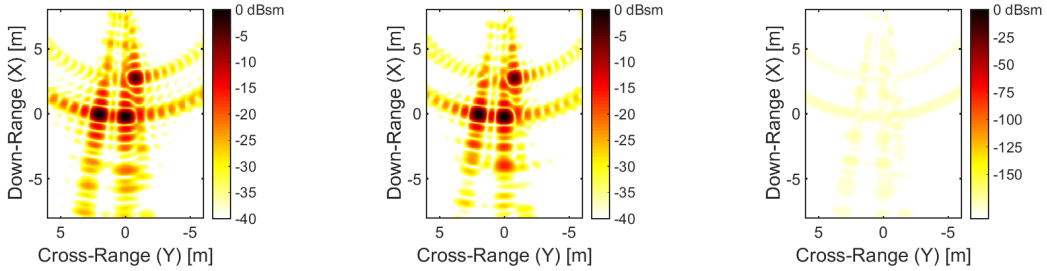

(a) Zero Doppler shift introduced.

(b) Exaggerated Doppler shift introduced.

(c) Difference image of (a) and (b).

Figure 21. SAR images created of the simulated scene in Fig. 19 to investigate the effects of introducing an exaggerated Doppler shift.

To investigate the possible effects on SAR images from large Doppler shift introduction, a test case is conducted where an 'exaggerated' Doppler shift is calculated by assigning a typical airborne receiver velocity of $v_{\mathrm{Rx}} = 600$ km/h ≈ 166.67 m/s. The exaggerated Doppler shift is then calculated using (28), with v_{Rx} being the only change from the results in Table 2 and Fig. 20. The zero Doppler, exaggerated

Doppler and difference images are shown in Fig. 21 for comparison.

Observing Fig. 21(b) shows that the exaggerated Doppler shift has limited effects on the final SAR image to the naked eye. Only when observing the difference image in Fig. 21(c) is the increased down-range ringing and minor cross-range warping of the target response sidelobes visible. The dBsm scale of Fig. 21(c) is consistent with that of Fig. 20(c), showing that in both cases, image error from Doppler shift is negligible with the majority of image error < -160 dBsm. As discussed by considering Fig. 20, and Fig. 21 with an exaggerated v_{Rx}, Doppler is not considered a significant error source in this research, so this research shifts to investigating and compensating for MMEs. The simulation tool developed for this research, however, enables robust Doppler shift simulation and can be extended to investigate further SAR imaging scenes or introduce multiple moving platforms to find cases where Doppler shift distortion is a significant consideration.

4.2 Motion Measurement Errors

As described in Chapter III, the preliminary testing methodology used for the outdoor experimental results presented in this chapter uses the original software interface from [9] . This original software interface has the drawback that acquisition commencement and receiver motion commencement are triggered by 'simultaneous' button clicks by the user, with the caveat being that the accuracy of the collection timing is down to the ability of the operator and is thus not perfectly repeatable across all experiments. The human factor present in this methodology can cause error in start synchronisation between the oscilloscope capture and the receiver motion, thus resulting in a position difference between actual pulse collection and the position used in the BPA.

4.2.1 Pulse Dropping.

A key assumption is that the receiver speed is uniform across the entire collection aperture, which manifests in 'ideal' pulse position estimates. Dropping pulses during the speed changing zones at either end of the collection aperture should remove any major phase distortion and leave only a possible constant offset in position estimation. However, when dropping pulses, there will be a small change in cross-range resolution that occurs due to the smaller collection azimuth extent. In order to investigate results after dropping pulses from each end of the collection, the ability for pulse selectivity was integrated into signal processing routines. The results presented next can be viewed in relation to the outdoor experimental results presented in Section 3.2.2, where the configuration is identical but with zero pulses dropped from the collection.

4.2.1.1 Half-length Signal Collection.

For the LTE11, DVB2 and DAB11 signals presented in Section 3.2.2, 32 pulses were captured across the entire collection. In order to enable comparison with a collection of 16 longer signal pulses, the number of pulses dropped at each end of the collection is incremented in multiples of two here. For a DVB2 signal with $v_{\mathrm{Rx}} = 0.1$ m/s, results can be seen in Fig. 22, whilst results for an LTE11 signal with $v_{\mathrm{Rx}} = 0.4$ m/s can be seen in Fig. 23.

Both Figs. 22 and 23 show how effectively pulse dropping can refine target responses, with both examples showing significant distortion removal. However, due to target C's position at $y = -2$, the higher power responses are at the end of the track and have been removed through the pulse dropping process, thus rendering target C invisible as more pulses are dropped. Additionally, once enough pulses are dropped, the cross-range resolution of the SAR image becomes degraded due to the lowered aperture extent, as particularly noticeable when comparing Figs. 22(c) and 22(d).

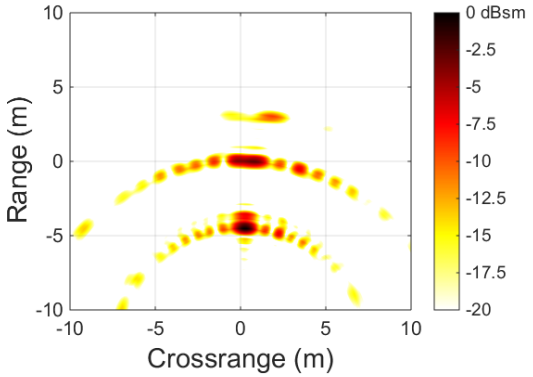

(a) SAR image with four (two at each end) of 32 pulses dropped.

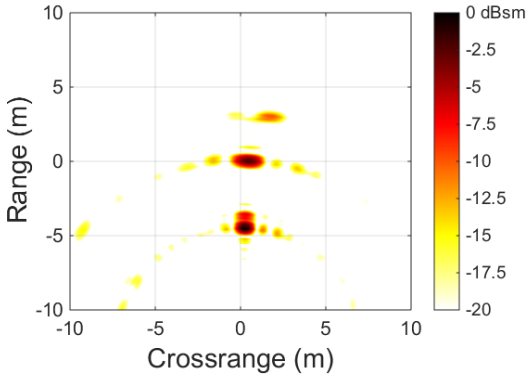

(b) SAR image with eight (four at each end) of 32 pulses dropped.

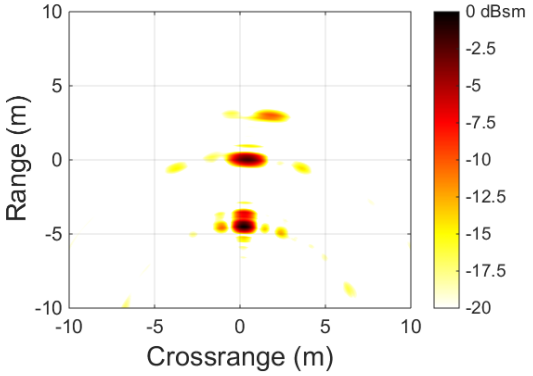

(c) SAR image with 12 (six at each end) of 32 pulses dropped.

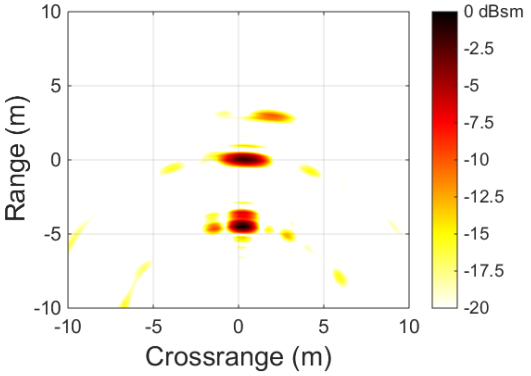

(d) SAR image with 16 (eight at each end) of 32 pulses dropped.

Figure 22. SAR images using a DVB2 signal, $v_{\mathrm{Rx}} = 10$ cm/s and various numbers of dropped pulses.

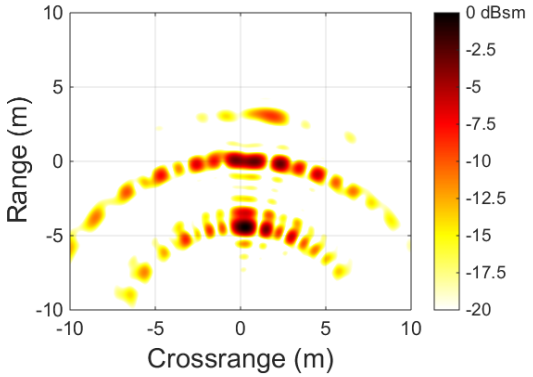

(a) SAR image with four (two at each end) of 32 pulses dropped.

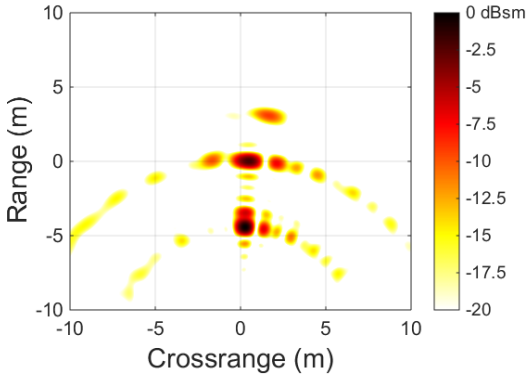

(b) SAR image with eight (four at each end) of 32 pulses dropped.

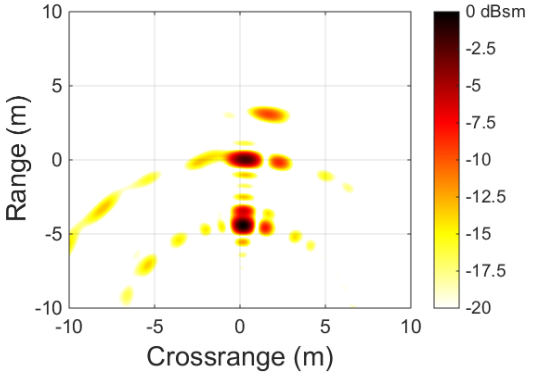

(c) SAR image with 12 (six at each end) of 32 pulses dropped.

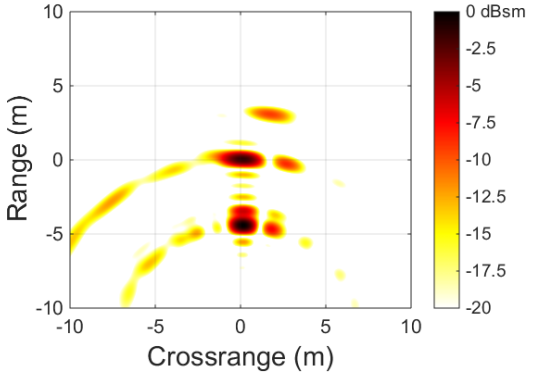

(d) SAR image with 16 (eight at each end) of 32 pulses dropped.

Figure 23. SAR images using a LTE11 signal, $v_{\mathrm{Rx}} = 40$ cm/s and various numbers of dropped pulses.

4.2.1.2 Full-length Signal Collection.

For the LTE23, DV5 and DAB23 signals presented in Section 3.2.2, 16 pulses were captured across the entire collection and further results are obtained by dropping one pulse from each end of the collection at a time. For a DVB5 signal with $v_{\mathrm{Rx}} = 0.1$ m/s and $v_{\mathrm{Rx}} = 0.4$ m/s, results can be seen in Fig. 24, whilst results for an LTE23 signal with $v_{\mathrm{Rx}} = 0.4$ m/s, results can be seen in Fig. 25.

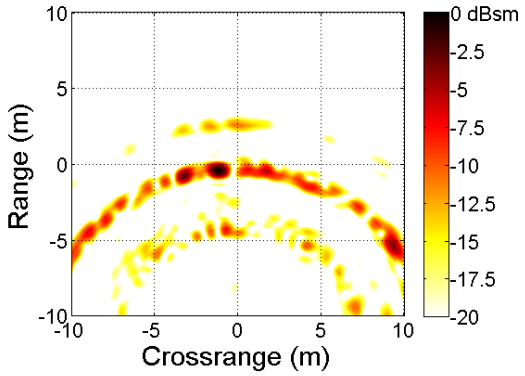

(a) SAR image with two (one at each end) of 16 pulses dropped.

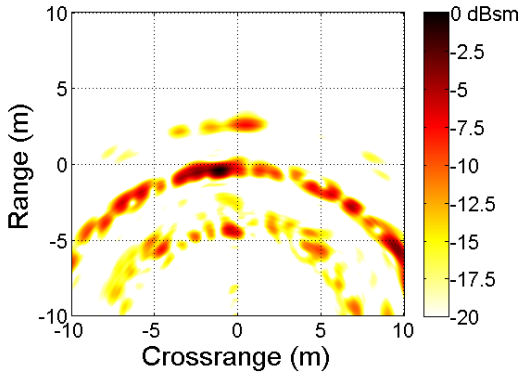

(b) SAR image with four (two at each end) of 16 pulses dropped.

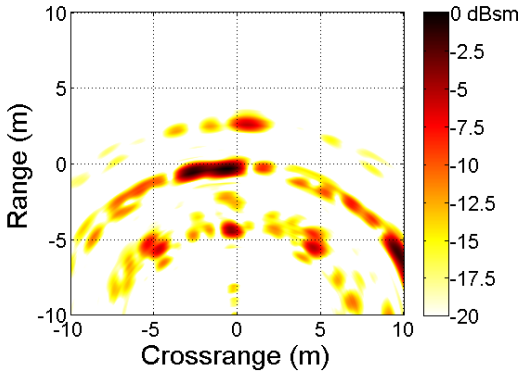

(c) SAR image with six (three at each end) of 16 pulses dropped.

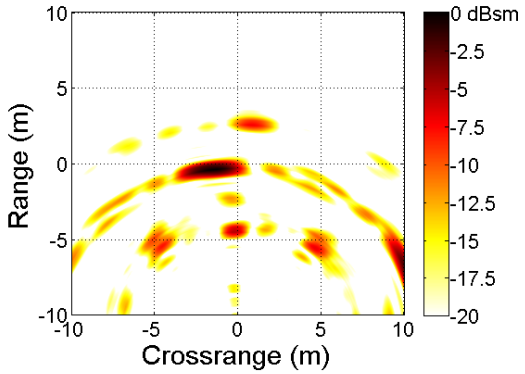

(d) SAR image with eight (four at each end) of 16 pulses dropped.

Figure 24. SAR images using a DVB5 signal, $v_{\mathrm{Rx}} = 10$ cm/s and various numbers of dropped pulses.

Again, Figs. 24 and 25 show how effectively pulse dropping can refine target responses but with the tradeoff of reducing cross-range resolution and removing target responses at the end of the aperture. Considering pulse dropping in both half-length

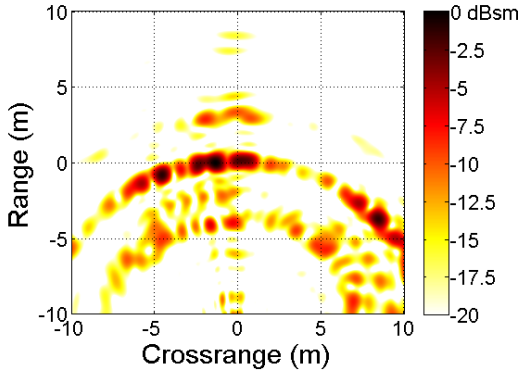

(a) SAR image with two (one at each end) of 16 pulses dropped.

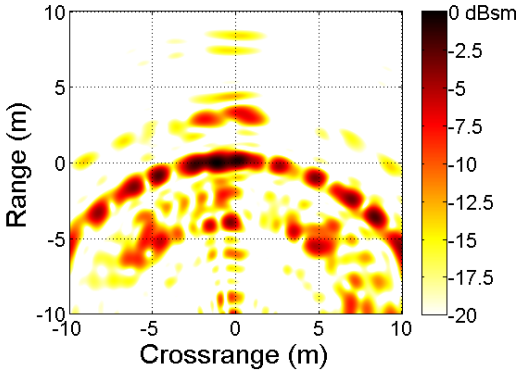

(b) SAR image with four (two at each end) of 16 pulses dropped.

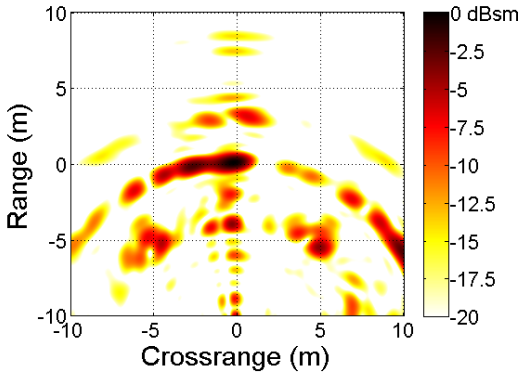

(c) SAR image with six (three at each end) of 16 pulses dropped.

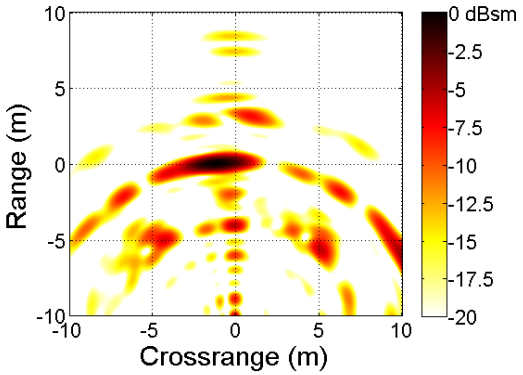

(d) SAR image with eight (four at each end) of 16 pulses dropped.

Figure 25. SAR images using a LTE23 signal, $v_{\mathrm{Rx}} = 40$ cm/s and various numbers of dropped pulses.

and full-length experimental results, it can be seen that dropping 3/8 of pulses consistently gives the best tradeoff between removing image distortion and retaining target response fidelity. Retaining 5/8 of pulses gives the results seen in Figs. 22(c), 23(c), 24(c) and 25(c).

4.2.2 Computer Processing Time and Pulse Position Analysis.

Using the updated experimental system of Chapter III for indoor experimentation allows characterisation of the known sources of error within the system, such as processing times and processing order. In an effort to remove MMEs, it is desirable

to extract the actual pulse collection positions from the test system during collection. One method where the receiver position is constantly queried and matched to pulse timings was attempted but this was proven to be too computationally intensive with the current (outdated) laptop computer to render accurate results. It was found that, whilst obtaining a receiver velocity vector was achievable, the processing overhead in querying the motor delayed the start of records by an unknown amount, thus making accurate pulse position matching unachievable. As such, a position estimation technique using characterisation of processing times is presented as follows.

Firstly, the order of operations within the Matlab code execution was analysed to determine key events. It was found that the two key events were that of triggering the linear track to commence motion and that of triggering the RF collection, which involves both starting AWG transmission and triggering the oscilloscope FastFrame$^{\text{TM}}$ collection. Using Matlab `tic` and `toc` functions, the two processes were timed across 60 trials each to ensure adequate convergence to a cumulative mean processing time. Each trial was conducted independently following completion of the previous trial, with only Matlab and one Windows Explorer window running in each instance. Fig. 26 shows the results of the 60 trials for each process resulting in the following mean and standard deviation values:

- *Triggering RF collection.* Total mean processing time across both processes of 1.63 ± 0.47 seconds.

- *Triggering receiver motion.* Total mean processing time of 7.99 ± 0.13 milliseconds.

The two possible constructs of triggering the moving collection are to trigger motion first and then start RF collection, or vice versa. Using the mean processing times and standard deviations across the trials observed above, pulse positions are estimated using a sequential timing approach, with calculation of positions within

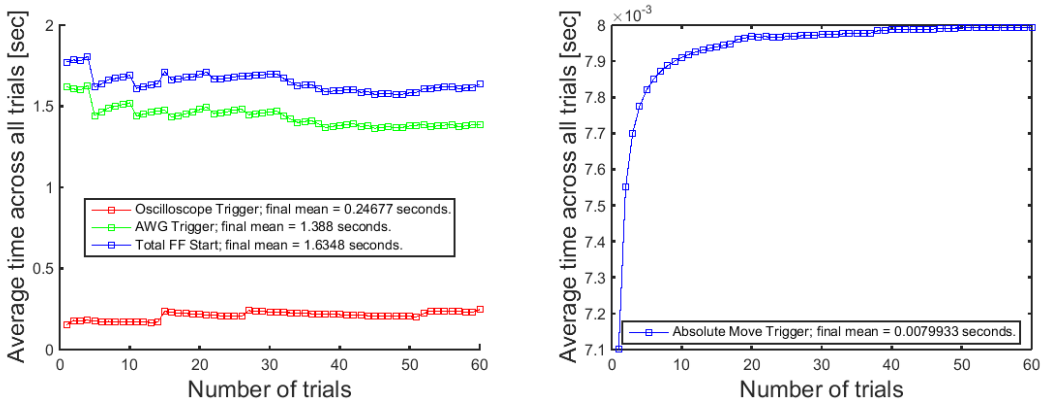

(a) RF collection (b) Motion commencement

Figure 26. Mean processing time to trigger certain operations, showing convergence over 60 trials.

the acceleration and deceleration zones included, as described below. As stated in Section 2.1.2.1, the experimental methodology of this research uses a single receiver velocity and, therefore, there is only one acceleration and one deceleration zone in contrast to the example shown earlier in Fig. 2. Position estimates are calculated using the assumptions that the receiver linearly accelerates over the programmed $t_{\text{acc}} = t_{\text{dec}} = 0.5$ seconds and achieves the required constant velocity, v_{Rx}, that the signal PRI is accurately generated from the AWG and that t_{echo} is sufficiently negligible for the small-scale experimental scenes under test. Using the time-velocity profile, $\psi(t)$, position estimates are calculated in the following three regions:

1. *Receiver Acceleration*: This region spans t_{acc} during which time the receiver is accelerating to its travel speed. Firstly, pulse timestamps, t_p, are generated for each pulse using the signal PRI and processing time for triggering RF collection, where $t = 0$ is the end of triggering RF calculation, as per the result of Fig. 26(a). Any pulse timestamps within $t \in [0, t_{\text{acc}}]$ are considered within the acceleration zone. During the acceleration region, pulse position is estimated as $y_p = \int_0^{t_p} \psi(t)dt$.

2. *Receiver Constant Velocity*: Pulse timestamps that fall within the region $t \in [t_{\text{acc}}, t_{\text{collection}} - t_{\text{dec}}]$ are considered within the constant velocity region. This region spans the majority of the linear track during which time the receiver is moving at a known speed with zero acceleration so position estimates are calculated as $y_p = \int_0^{t_p} \psi(t)dt = y_{\text{acc}} + (t_p - t_{\text{acc}})v_{\text{Rx}}$, where $y_{\text{acc}} = \int_0^{t_{\text{acc}}} \psi(t)dt$ is the total distance covered during the acceleration region.

3. *Receiver Deceleration*: This region spans $t \in [t_{\text{collection}} - t_{\text{dec}}, t_{\text{collection}}]$, during which time the receiver is decelerating to stationary. In this region, pulse positions are calculated as $y_p = \int_0^{t_p} \psi(t)dt = D - \int_{t_{\text{collection}}-t_p}^{t_{\text{collection}}} \psi(t)dt$.

Fig. 27 shows pulse position estimates using both algorithm construct options across all receiver velocities, v_{Rx}, and Fig. 28 shows the total collection extents, i.e., synthetic aperture size, for both methods as a function of v_{Rx}. Positions were calculated at the mean processing times from Fig. 26 with error bars indicating position estimates recalculated at ± 1 standard deviation from the mean processing time. Collection extents were calculated using the same mean and standard deviation values.

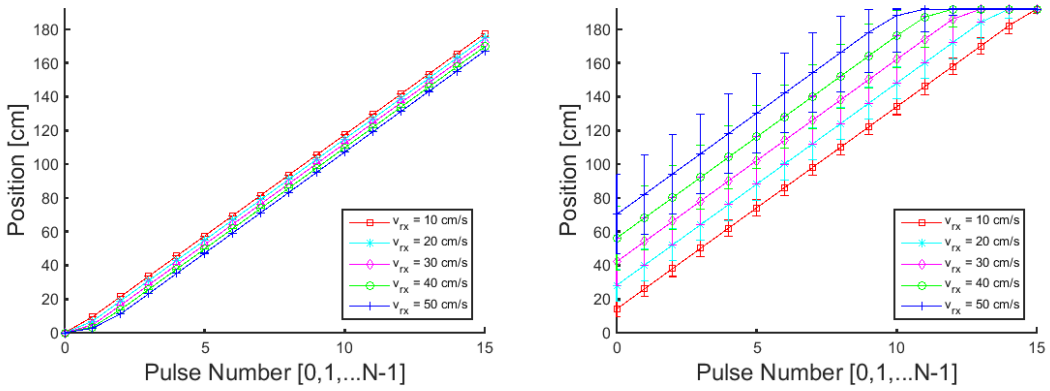

(a) Triggering RF collection first.

(b) Triggering receiver motion first.

Figure 27. Estimated received pulse positions for alternate processing constructs with different v_{Rx}. Error bars indicate position estimate limits at ± 1 standard deviation of processing time.

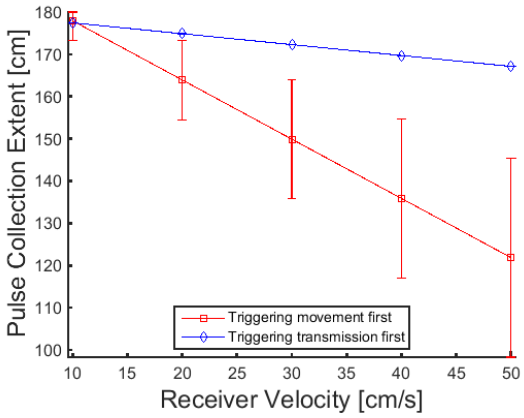

Figure 28. Estimated synthetic aperture extents across various v_{Rx} using alternate processing constructs.

As shown in both Figs. 27 and 28, the order of processing operation does affect pulse positions and total azimuthal coverage. It is shown that the larger processing time variance for triggering motion greatly degrades the accuracy of position estimates in Fig. 27(b), particularly at higher receiver velocities. Additionally, the larger mean processing time for triggering motion results in a position estimate for pulse 0 that is much further along the track than for triggering motion first due to the time to trigger RF capture whilst the the receiver is accelerating. The summary of collection extents in Fig. 28 shows that the burden of triggering motion results in a much smaller effective synthetic aperture size, particularly at high v_{Rx} values.

When RF capture is triggered first, however, it can be seen in Fig. 27(a) that multiple pulses can be collected at the first position (dependant upon how small the PRI is) but that position estimates are substantially more accurate as the receiver position can be accurately calculated through acceleration and travelling velocity after the processing time to start motion. As triggering RF collection first proves to be the less variable algorithm construct and provides a larger collection extent, all collections using the software interface of Section 3.3 are programmed to trigger RF collection first. The position estimate models of Fig. 27(a) for all receiver velocities will be

used during signal processing to obtain final experimental results in Section 4.3.4.

4.2.3 Simulation of MME.

In an attempt to explain the anomalies seen in the experimental results obtained, where Doppler shift has previously been shown to be insignificant, MMEs can be inserted into a scene simulation. MMEs are simulated by using one receiver position vector for differential range calculation during phase-history production and a slightly altered position vector for differential range calculation within the BPA. Using the ideal pulse position vector, $y_p = [-0.96 : 0.12 : 0.84]$ m, and the two position estimates from Fig. 27 for $v_{\text{Rx}} = 0.5$ m/s, the MME affected images of Figs. 29 and 30 are created.

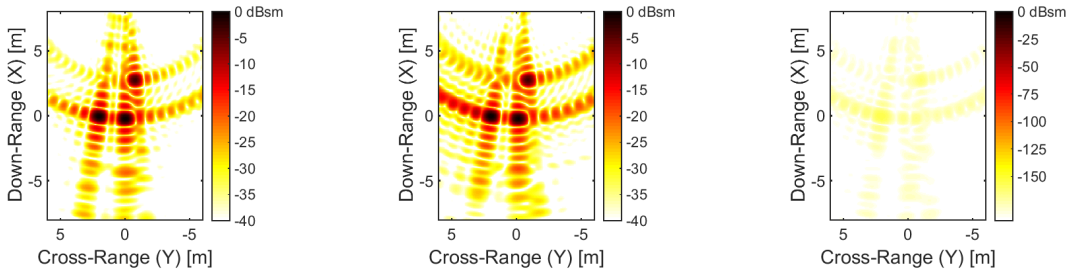

(a) Zero MMEs.

(b) MMEs introduced using estimated pulse positions from Fig. 27(a).

(c) Difference image of introduced MMEs and zero MMEs.

Figure 29. Comparison of simulated SAR images with no position error and with MME using the estimated pulse positions when triggering RF collection first.

Using the position estimates that more closely align with the ideal pulse positions, i.e., the estimates when triggering RF collection first, Fig. 29 shows that the small MMEs present contribute to a cross-range blurring of the image, which is particularly noticeable in Fig. 29(c). Note that all errors displaced from the targets in the down-range direction are cross-range errors that have been bent around the respective target isorange contour. The reason that only cross-range blurring occurs in simulation of the outdoor experimental scene is because the receiver only moves in the cross-range

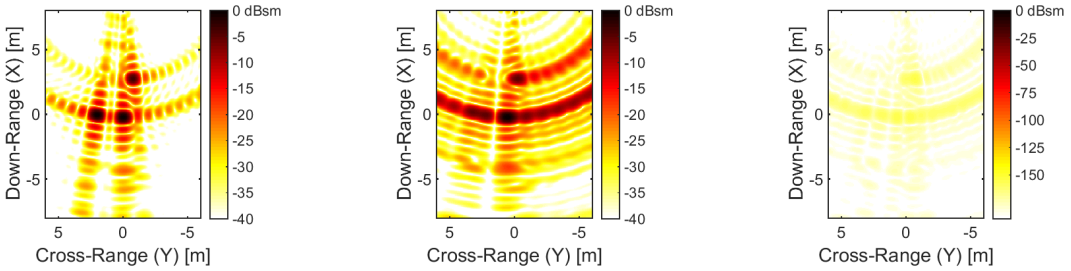

(a) Zero MMEs.

(b) MMEs introduced using estimated pulse positions from Fig. 27(b).

(c) Difference image of introduced MMEs and zero MMEs.

Figure 30. Comparison of simulated SAR images with no position error and with MME using the estimated pulse positions when triggering receiver motion first.

dimension and all other aspects of the scene are fixed, thus removing other possible areas of MMEs when assuming perfect knowledge of the range and height positions of the antenna. In comparison to Fig. 20, it can be seen that the introduction of small MMEs has a larger effect on the final SAR image than that of the calculated Doppler shifts present in the experimental collection, thus justifying MME as the choice for error compensation. Observing Fig. 30 confirms that a larger cross-range position error results in much larger cross-range blurring, but that down-range accuracy is relatively unaffected, as shown in Fig. 30(c) by the dark segments in line with target positions.

4.2.4 MME Analysis.

As described in Chapter II, the low frequency MME components can be expressed in polynomial form using (15). In order to explain the experimental and simulation results seen thus far and estimate expected MME, the development of [26, p.370-380] and [27] is extended with consideration to the AFIT RAIL RF collection system. Firstly, (15) can be simplified by using assumptions relevant to the experimental system under test. Assuming flat ground for track installation and accurate alignment of the track in the cross-range and vertical direction, the only areas for error can occur

in cross-range position, velocity and acceleration. Removing down-range and vertical error, the error polynomial of (15) can be modelled as

$$\tilde{g}_y(\tau) = \tilde{p}_y + \tilde{v}_y\tau + \tilde{a}_y\frac{\tau^2}{2} \tag{29}$$

where $\tilde{p}_y$, $\tilde{v}_y$ and $\tilde{a}_y$ are the cross-range position, velocity and acceleration errors respectively and $\tau = [0, t_1, \ldots, t_{P-2}, t_{\text{collection}}]$. The error function is calculated in the three receiver motion regions previously established as follows:

1. *Receiver Acceleration*: There is the potential for position, velocity and acceleration error in this transition region due to lack of synchronisation between starting pulse collection and receiver motion, as well as the unknown accuracy and lack of accountability for receiver acceleration in pulse positioning setup. However, as receiver acceleration is taken into account through the position estimation development in Section 4.2.2, both $\tilde{v}_y$ and $\tilde{a}_y$ have been minimised. As linear acceleration is assumed, $\tilde{a}_y = 0$ m/s^2 is chosen. Velocity error is chosen to align with one standard deviation in triggering RF collection offsetting the velocity slope in $\psi(t)$, thus giving $\Delta t = 0.13$ ms and $\tilde{v}_y = 1.13 \times 10^{-3}$ m/s. Lastly, $\tilde{p}_y = D/P = 1.92/16 = 0.12$ m is chosen to reflect the collection of $P = 16$ pulses.

2. *Receiver Constant Velocity*: In this region, a step size position error of $\tilde{p}_y = 0.12$ m is maintained whilst a velocity error of $\tilde{v}_y = 0.325 \times 10^{-3}$ m/s is chosen to align with the programmed resolution of the motor step controller [9, 47]. Lastly, due ot the constant velocity in this region, $\tilde{a}_y = 0$ is maintained.

3. *Receiver Deceleration*: In this region, equal assumptions for position, velocity and acceleration errors are made as in the receiver acceleration region, i.e., $\tilde{p}_y = 0.12$ m, $\tilde{v}_y = 1.13 \times 10^{-3}$ m/s and $\tilde{a}_y = 0$ m/s^2.

Using these system error values in (29), error functions are created for each region by following the process of [26, p.370-380], as shown in Fig. 31. Each receiver motion region is divided into three subaperture estimates, although this is unapparent in Fig. 31 due to the linear nature of the piecewise functions. An image domain estimate of a target can be calculated as [26, p.377]

$$\begin{bmatrix} \hat{x}_i \\ \hat{y}_i \end{bmatrix} = Q_i^{-1} \begin{bmatrix} \vartheta_{0,i} + \tilde{\vartheta}_{0,i} \\ \vartheta_{1,i} + \tilde{\vartheta}_{1,i} \end{bmatrix} \tag{30}$$

$$= \begin{bmatrix} x_i \\ y_i \end{bmatrix} + Q_i^{-1} \begin{bmatrix} \tilde{\vartheta}_{0,i} \\ \tilde{\vartheta}_{1,i} \end{bmatrix} \tag{31}$$

$$\triangleq \begin{bmatrix} x_i \\ y_i \end{bmatrix} + \begin{bmatrix} \tilde{x}_i \\ \tilde{y}_i \end{bmatrix} \tag{32}$$

where x_i, y_i are the actual target locations; $\tilde{x}_i$, $\tilde{y}_i$ are the target estimate errors; and Q_i is the linear mapping approximation of the differential range via the error intercept, $\vartheta_{0,i}$, and slope, $\vartheta_{1,i}$, for each of the i subapertures[3] (or line approximations) in a given region. Matrix Q_i and its inverse are defined as [26, p.379]

$$Q_i = \begin{bmatrix} -\frac{x_t(\tau_i)}{R_t} + \frac{x_r(\tau_i)}{R_r} & -\frac{y_t(\tau_i)}{R_t} - \frac{y_r(\tau_i)}{R_r} \\ -\frac{v_{xt}}{R_t} - \frac{v_{xr}}{R_r} & -\frac{v_{yt}}{R_t} - \frac{v_{yr}}{R_r} \end{bmatrix} \tag{33}$$

$$Q_i^{-1} = \frac{1}{|Q_i|} \begin{bmatrix} -\frac{v_{yt}}{R_t} - \frac{v_{yr}}{R_r} & \frac{y_t(\tau_i)}{R_t} + \frac{y_r(\tau_i)}{R_r} \\ \frac{v_{xt}}{R_t} + \frac{v_{xr}}{R_r} & -\frac{x_t(\tau_i)}{R_t} + \frac{x_r(\tau_i)}{R_r} \end{bmatrix} \tag{34}$$

where R_t and R_r are the slant ranges to the target from the transmitter and receiver respectively.

[3]The development in [26, p.370-380] defines the slope and intercept of the differential range approximation as $\beta_{0,i}$ and $\beta_{1,i}$ respectively, but the notation has been changed to $\vartheta_{0,i}$ and $\vartheta_{1,i}$ in this thesis to avoid confusion with the bistatic angle, β.

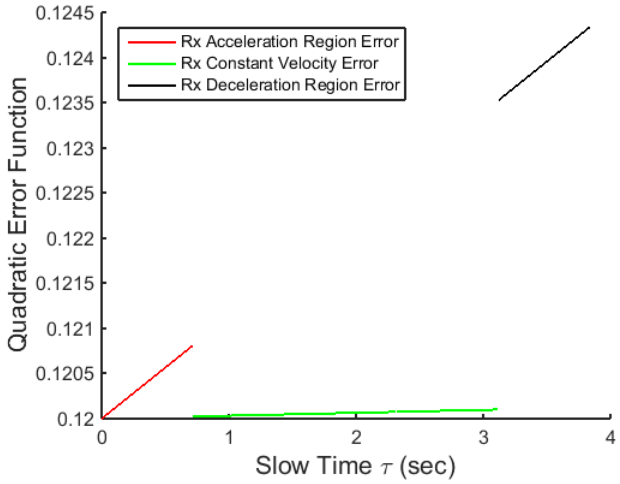

Figure 31. Piecewise quadratic function, induced by system error. Created using three receiver motion regions in the experimental scene of Fig. 9, each with three subapertures.

Using the three subaperture midpoints of each receiver motion region in Fig. 31 as reference points, nine image domain responses can be estimated using (31). Following the process of [26, p.370-380], image domain estimates for target A at $(x_i, y_i) = (0, 0)$ are shown in Fig. 32. Observing Fig. 32 shows two main clusters of image domain estimates, based upon the receiver region under analysis. It can be seen in Fig. 32 that the minute velocity error and zero acceleration error during the *receiver constant velocity* region leads a down-range error of $\tilde{x}_i \approx 0.06$ m and $\tilde{y}_i \approx 1 \times 10^{-3}$ m cross-range error. The larger velocity error present during the other two regions increases cross-range error to $\tilde{y}_i \approx 0.03$ m whilst the down-range error remains consistent at $\tilde{x}_i \approx 0.06$ m.

It is important to note that (31) is spatially invariant, i.e., the estimation error does not vary with the actual target location within the scene but remains constant centred at the actual target location. The cross-range errors in the image domain point estimate can lead to blurring in the final SAR image as point estimates start to overlap each other. The results in Fig. 32 suggest that any use of the AFIT RAIL RF collection system, even when implementing pulse position estimation, is subject

to blurring up to 0.06 m in the down-range direction and up to 0.03 m in the cross-range direction simply due to MMEs. This target blurring will contribute to target responses extending beyond their theoretical resolution, as is evident in the measured outdoor experimental resolutions presented in Section 3.2.2. To investigate the final effect of the predicted MMEs on an image, an ideal target point response will be considered along with final experimental results in the next section.

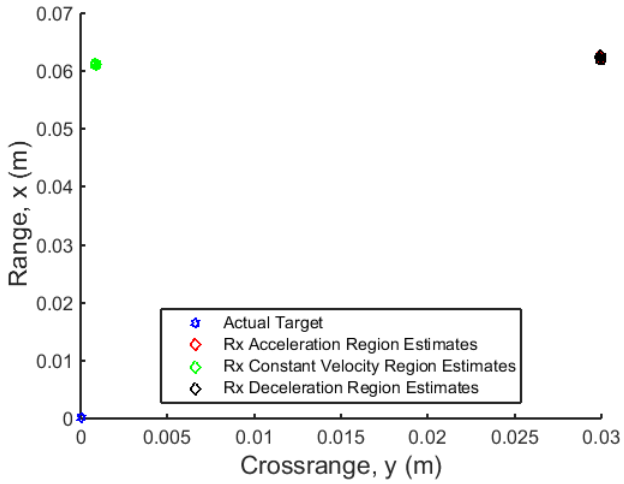

Figure 32. Approximate image domain locations corresponding to a error approximation corresponding to $\tilde{p}_y = 0.12$ m, $\tilde{v}_y = 0$ or 0.01 m/s and $\tilde{a}_y = 0$ m/s^2.

4.3 Indoor Experimental Scene

4.3.1 Experimental Configuration.

Once results were obtained on the outdoor scene, experiments were designed within the laboratory for a much smaller scene. These indoor experiments were designed to capture data from a single target and to test error compensation methods. For indoor experimentation, $D = 1.92$ m and $v_{\text{Rx}} \in \{0.1, 0.2, 0.3, 0.4, 0.5\}$ m/s are still used. However, as shown in Fig. 33, the indoor scene involves a single stationary vertical cylinder target to give a rounded edge for maximum reflection across the synthetic aperture. As the target of Fig. 33 is within the $S = 7.22$ m Fresnel parameter

calculated in Section 3.2.1, near-field processing is again used during backprojection.

In the indoor experimental configuration, the centre of the receiver aperture is again at the same azimuthal position as the transmitter, meaning that the expected resolution values are approximated using $\Delta\phi = 2\tan^{-1}(0.5D/R_R) = 2\tan^{-1}(0.96/2.9)$ $\approx$ 0.6394 radians to give

$$\rho_x = \frac{c}{2B} = 0.4997 \text{ m}, \tag{35}$$

$$\rho_y = \frac{\lambda}{2\Delta\phi} = 0.0938 \text{ m}. \tag{36}$$

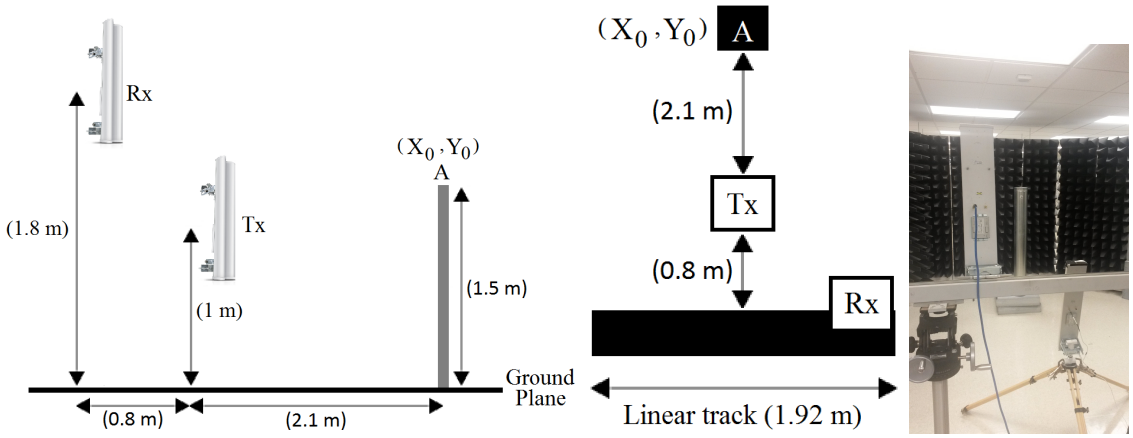

(a) Side view. (b) Top view. (c) Photo view.

Figure 33. Indoor Experimental Scene Configuration at the AFIT RAIL.

The software interface development described in Section 3.3 was carried out using the indoor experimental setup of Fig. 33 in order to test interface features as they were developed. Once software interface development was completed, final testing was conducted using this indoor experimental scene. Results from final testing on this indoor experimental scene will be discussed below.

4.3.2 Doppler Analysis.

To ensure the limited impact of Doppler shift is still valid on the indoor experimental scene of Fig. 33, the Doppler shifts are again calculated as per Section 4.1, but with the updated experimental configuration. The increased elevation difference between the transmitter and receiver has increased the 3D bistatic angle for the indoor experimental scene, thus slightly increasing the Doppler shift values to those listed in Table 3. The maximum absolute Doppler shift present in the indoor experimental scene is approximately 1.39 Hz (when $v_{\mathrm{Rx}} = 0.5$ m/s) and the maximum discrepancy between the frequency extremes of the bandwidth is less than 0.16 Hz (at $v_{\mathrm{Rx}} = 0.5$ m/s).

Table 3. Bistatic Doppler shift calculation for various receiver positions in the indoor scene configuration of Fig. 33.

v_{Rx} (m/s)	Rx Start Position		Rx Mid Position		Rx End Position	
	@f_{min}	@f_{max}	@f_{min}	@f_{max}	@f_{min}	@f_{max}
0.1	0.2463 Hz	0.2778 Hz	0 Hz	0 Hz	-0.2778 Hz	-0.2463 Hz
0.2	0.4927 Hz	0.5556 Hz	0 Hz	0 Hz	-0.5556 Hz	-0.4927 Hz
0.3	0.7390 Hz	0.8334 Hz	0 Hz	0 Hz	-0.8334 Hz	-0.7390 Hz
0.4	0.9854 Hz	1.1112 Hz	0 Hz	0 Hz	-1.1112 Hz	-0.9854 Hz
0.5	1.2317 Hz	1.3890 Hz	0 Hz	0 Hz	-1.3890 Hz	-1.2317 Hz

The "fan blades" present in Figs. 34(a) and 34(a) are due to the target sidelobes being compressed in the cross-range direction (due to resolution improvement) and being curved along the radar wavefront (due to the use of near-field processing). Whilst the Doppler shifts have increased due to the geometry of the indoor experimental configuration, Fig. 34, shows that the simulated effects of Doppler shift on the final SAR image have actually decreased from the results shown in Fig. 20 for the outdoor scene, with all image error below the difference image dynamic threshold. This counter-intuitive result is partially explained by the adjusted image bounds for the indoor scene, where most of the Doppler ringing of the outdoor scene is outside the visible extents of the indoor SAR image. Additionally, the calculated Doppler shifts

in Table 3 are still minimal that negligible Doppler effects are predicted. As such, MMEs will still be the focus of error correction for results on the indoor experimental scene.

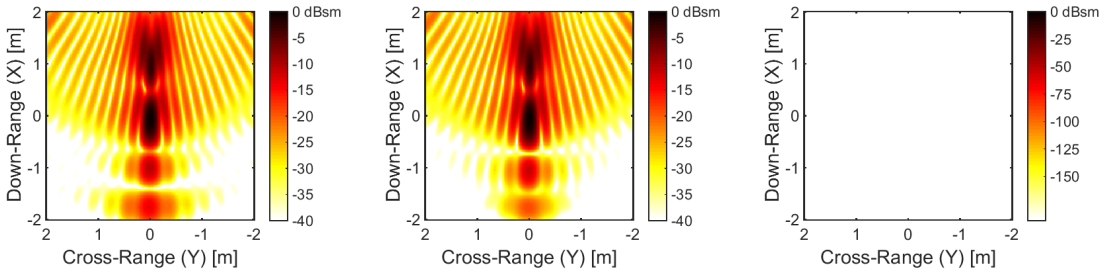

(a) Zero Doppler shift introduced.

(b) Theoretical Doppler shifts of Table 3 introduced.

(c) Difference image of theoretical Doppler shifts of Table 3 and zero Doppler shift.

Figure 34. Various simulated SAR images using the scene configuration of Fig. 33 with different Doppler shift values.

4.3.3 Point Target Response Analysis.

Before presenting final experimental results, a point target response for the indoor experimental scene will be considered in order to analyse system behaviour in relation to the estimated MME induced error calculated in Section 4.2.4. The point target responses shown in Fig. 35 represent the ideal image formed for a point target present at the scene centre, given the collection geometry of Fig. 33 and using the estimated pulse positions of Fig. 27(a) with either $P = 16$ or $P = 10$ pulses. Comparing the mainlobe response in Figs. 35(a) and 35(b) shows that dropping pulses and lowering the aperture extent, $\Delta\phi$, does indeed degrade cross-range resolution, ρ_y, whilst having no impact on down-range resolution, ρ_x.

Additionally, a minor clockwise rotation of each point response is visible, emphasised by the drop in resolution in Fig. 35(b). As the point response is ideally created using only the estimated pulse positions, this rotation is due to error between the ideal pulse positions and the estimated pulse positions, i.e., the rotation is due to

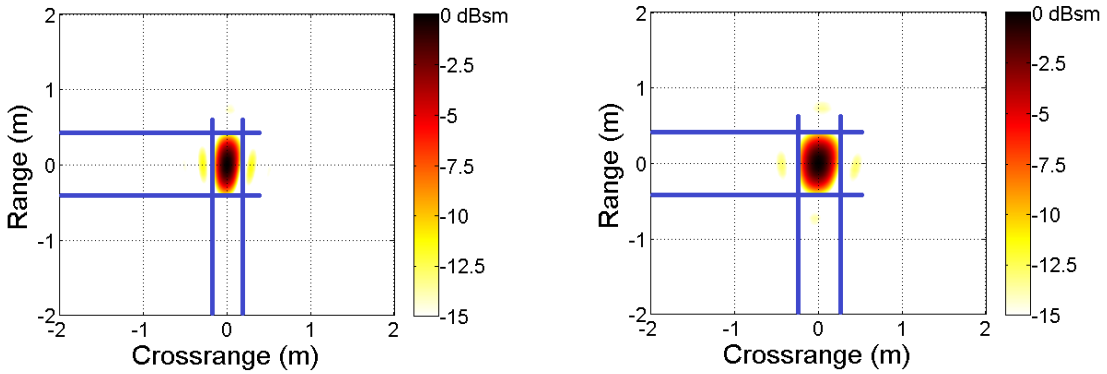

(a) $P = 16$ pulses. Resolution values of $\rho_x \approx 0.43$ m and $\rho_y \approx 0.16$ m.

(b) $P = 10$ pulses; three dropped at each end of the collection. Resolution values of $\rho_x \approx 0.43$ m and $\rho_y \approx 0.25$ m.

Figure 35. Ideal point target response for the indoor scene configuration of Fig. 33, using estimated pulse positions established in Section 4.2.2 with different P values.

MMEs along the collection aperture. As estimated in Section 4.2.4, some of the point target returns may be displaced by up to $\tilde{y}_i \approx 0.03$ m and $\tilde{x}_i \approx 0.06$ m, depending upon their region of collection. With these erroneous returns present in the 'north-east' and 'southwest' areas from the origin, the overlapping of all returns creates the slight rotation effect present in both point responses of Fig. 35.

Lastly, an effect of having non-uniform sampling along the synthetic aperture, as induced by the processing times analysed in Section 4.2.2, is that any target responses will have asymmetric sidelobes in the final SAR image. Whilst it is difficult to discern, the point responses in Fig. 35 do indeed have asymmetric sidelobes, with the top sidelobes being wider than the bottom sidelobes and the right sidelobes being taller than the left sidelobes. Despite considering both the target response rotation and the asymmetric sidelobes, there are still limited MME related artifacts predicted for experimental results using the updated SAR RAIL SAR system, with overall distortion of < 0.1 m. As such, final experimental results will next be presented to validate these predictions and overall system performance.

4.3.4 Experimental Results.

4.3.4.1 Signal Processing Methodology.

Final experimental results were obtained through use of various signal processing techniques after pulse collections were made on the indoor experimental scene of Fig. 33. All RF collections on the indoor experimental scene were made using $v_{\text{Rx}} \in \{0.1, 0.2, 0.3, 0.4, 0.5\}$ m/s and $P = 16$ of the full-length DAB23, DVB and LTE23 signal. Signal processing is conducted to remove image distortion and MMEs and to attempt to achieve results consistent with the theoretical error degradation analysis in Section 4.2.4. Final signal processing is conducted using the following process:

1. *Ideal Pulse Positions*: As per the signal processing for outdoor experimental results, preliminary results are constructed using the ideal pulse position vector of $y_p = [-0.96 : 0.12 : 0.84]$ m in the BPA.

2. *Pulse Position Estimates*: Using the timing based pulse position model derived in Section 4.2.2 for triggering RF collection first, the mean position estimates are stored for each operating velocity, v_{Rx}. The respective position estimates are loaded during processing and used in the BPA instead of the ideal pulse position vector used for the outdoor and preliminary indoor experimental results previously presented.

3. *Pulse Dropping*: As examined in Section 4.2.1, dropping pulses at each end of the aperture is effective at removing some image distortion. As all indoor experimental images are constructed using $P = 16$ full-length pulses, up to three pulses are dropped at each end of the aperture to determine the best image result.

4. *Background Removal*: As the indoor experimental scene of Fig. 33 is small-scale, there is a strong possibility of external clutter giving extraneous returns.

In order to eliminate background clutter as an error source, SAR 'images' were created for each receiver speed with no target present within the scene. The resultant image is subtracted from the target image constructed after dropping pulses to give a final SAR image. The ability to create an image of an 'empty' scene may not be possible in all SAR applications, but for change detection implementation or experimental investigation, this is a reasonable assumption.

4.3.4.2 Indoor Experimental SAR Images.

Whilst the signal processing techniques can be used on any signal type and receiver velocity, selected results are shown here to demonstrate the final capabilities of the AFIT RAIL RF collection system updated through this research. Fig. 36 shows results using a DAB23 signal at $v_{\mathrm{Rx}} = 0.1$ m/s whilst Figs. 37 and 38 show results for a DVB5 and LTE23 signal at $v_{\mathrm{Rx}} = 0.5$ m/s respectively.

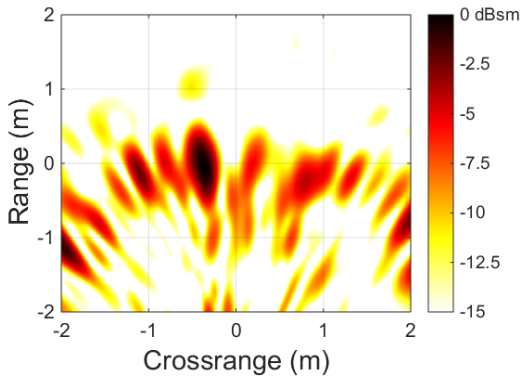

(a) SAR image created using ideal pulse position vector of $y_p = [-0.96 : 0.12 : 0.84]$ m.

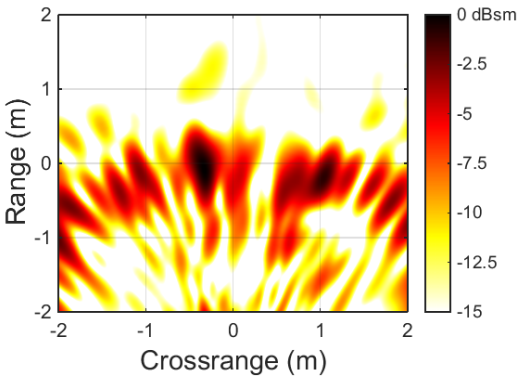

(b) SAR image created using estimated pulse positions established in Section 4.2.2.

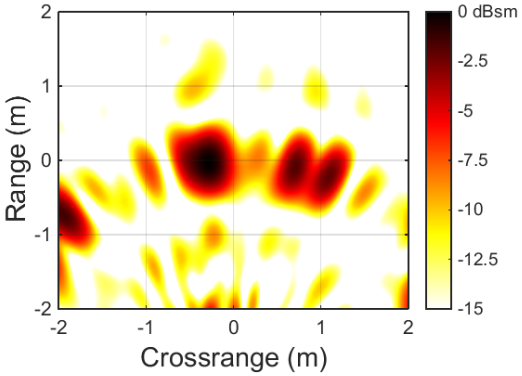

(c) SAR image created using estimated pulse positions and six (three at each end) of 16 pulses dropped.

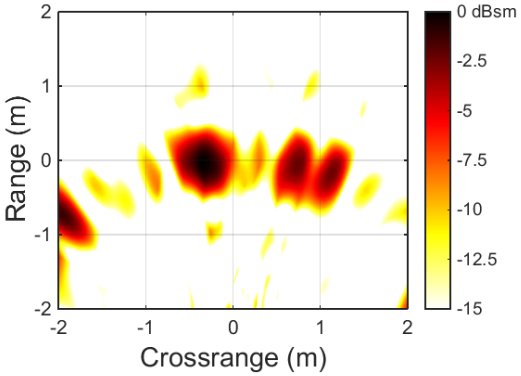

(d) SAR image created using estimated pulse positions, six of 16 pulses dropped and background clutter image removed.

Figure 36. SAR images created using various signal processing steps, a DAB23 signal and $v_{\mathrm{Rx}} = 10$ cm/s for the indoor experimental scene of Fig. 33.

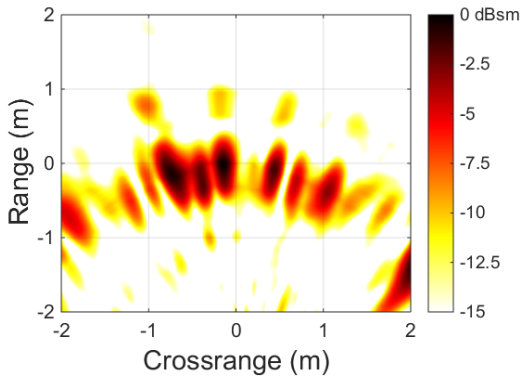

(a) SAR image created using ideal pulse position vector of $y_p = [-0.96 : 0.12 : 0.84]$ m.

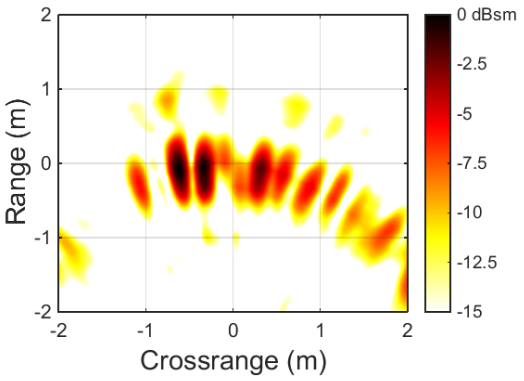

(b) SAR image created using estimated pulse positions established in Section 4.2.2.

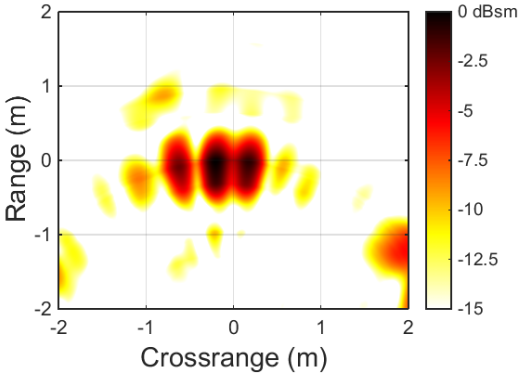

(c) SAR image created using estimated pulse positions and six (three at each end) of 16 pulses dropped.

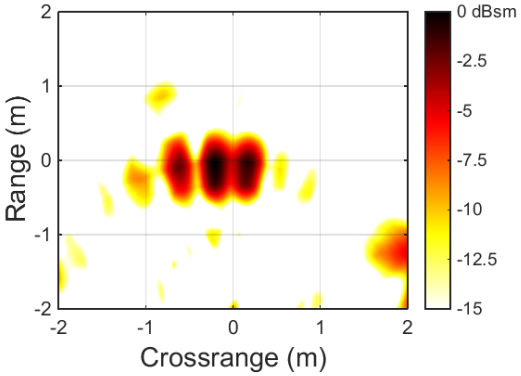

(d) SAR image created using estimated pulse positions, six of 16 pulses dropped and background clutter image removed.

Figure 37. SAR images created using various signal processing steps, a DVB5 signal and $v_{\mathrm{Rx}} = 50$ cm/s for the indoor experimental scene of Fig. 33.

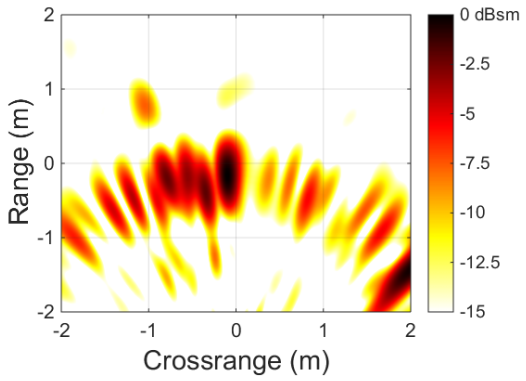

(a) SAR image created using ideal pulse position vector of $y_p = [-0.96 : 0.12 : 0.84]$ m.

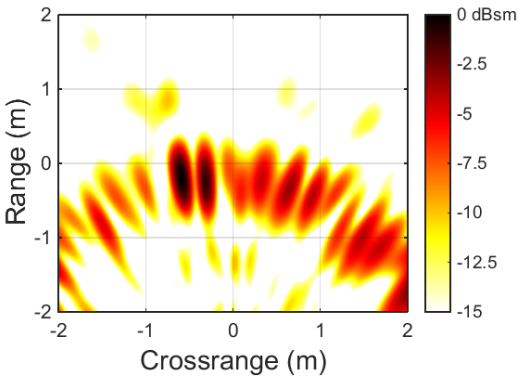

(b) SAR image created using estimated pulse positions established in Section 4.2.2.

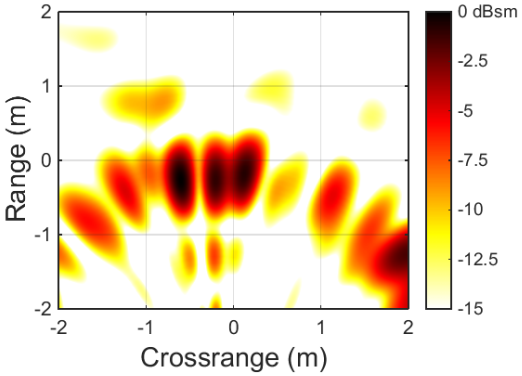

(c) SAR image created using estimated pulse positions and six (three at each end) of 16 pulses dropped.

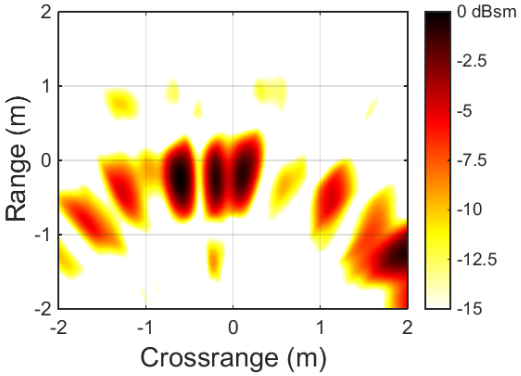

(d) SAR image created using estimated pulse positions, six of 16 pulses dropped and background clutter image removed.

Figure 38. SAR images created using various signal processing steps, a LTE23 signal and $v_{\mathrm{Rx}} = 50$ cm/s for the indoor experimental scene of Fig. 33.

4.3.4.3 Final SAR Image Analysis.

As per calculations made in Chapter III, the indoor experimental SAR images presented in Figs. 36 – 38 are constructed using near-field processing. For the indoor experimental scene, a single curved isorange contour is visible in all images due to the solitary target at the origin. Using a zoomed in image as previously, the estimated resolution cell is shown in Fig. 39. The measured down-range and cross-range resolutions for indoor testing are $\rho_x \approx 0.60$ m and $\rho_y \approx 0.23$ m. As with outdoor experimentation, the measured image resolution for the indoor experimental scene is degraded from the theoretical resolutions of $\rho_x = 0.4997$ m and $\rho_y = 0.0938$ m. It is noted that resolution estimation using manual determination of a resolution cell has inherent inaccuracies through human subjectivity of the point response zero crossing. Additionally, Figs. 36 – 38 show that dropping pulses on each end of the collection removes certain image anomalies but also degrades image resolution. Comparing the point response resolution values of Fig. 35(b) to those measured in Fig. 39 shows that the cross-range resolutions are approximately equal whilst the down-range resolution of the point response is better than the measured image. The difference in down-range resolution is due to the bandwidth of collection, where guard bands, i.e., zero padding in the frequency domain, in the OFDM signal lower the effective bandwidth of the signal whilst the full bandwidth of $B = 300$ MHz has been used in the frequency support of the target point response phase-history model.

Whilst the signal processing techniques implemented do improve overall image quality, each of the final images in Figs. 36(d), 37(d) and 38(d) still exhibit certain anomalies. As established through analysis of the point target response in Section 4.3.3, slight rotation of the main target lobe and asymmetric sidelobes are expected due to system MMEs.

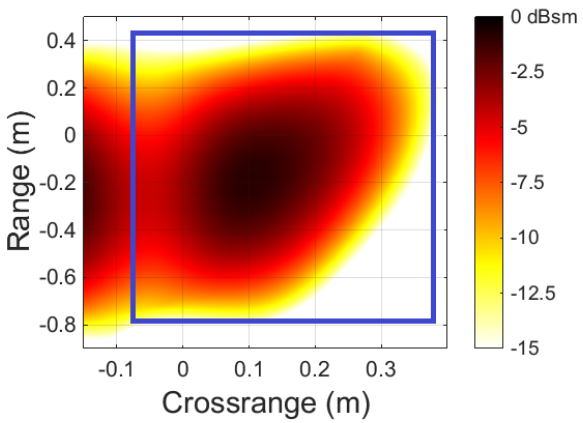

Figure 39. SAR image resolution measurement using the LTE23 image of Fig. 38(d). Down-range and cross-range resolutions measured as $\rho_x \approx 0.60$ m and $\rho_y \approx 0.23$ m respectively from centre of target.

However, the final SAR images exhibit distortions well in excess of those seen on a point target response. Likely sources of final image distortion include:

- *Target Choice*: As described in Section 4.3.1, a large vertical cylinder target was chosen to provide more uniform RF reflections across the entire synthetic aperture. However, the target is not a perfect cylinder and it is also much larger than the point targets used for analysis in in Section 4.3.3, therefore meaning that the predicted rotation and asymmetric sidelobes may be exacerbated in the final image.

- *Laboratory Clutter and Multipath*: As the experimental results were collected in a small laboratory environment with lots of other equipment lining the edges, there is a strong possibility that clutter and multi-path signals are creating erroneous target returns. Whilst some clutter effects have been removed through subtracting the background image, it is likely that there are multipath clutter returns that only occur when the target is present in the scene.

- *Invalid Assumptions*: As described throughout this thesis, multiple SAR collection assumptions were made to simplify image processing and error analysis. Primary assumptions that may be invalid in final SAR image creation are that the:
  - pulse positions estimated in Section 4.2.2 were based upon accurate processing times using Matlab's `tic` and `toc` functions; and
  - receiver track was accurately aligned in the cross-range direction and at a single elevation, thus ensuring the estimated MMEs are valid in only the cross-range direction.

The final experimental results of Figs. 36 – 38 show that the updated SAR RAIL SAR system is capable of measuring targets within a scene and constructing a SAR image through a variety of signal processing techniques. However, refinement is needed on the experimental scene and assumptions to create a pristine SAR image with more accurately predicted error behaviour.

4.4 RF Collection System Summary

It has been shown through experimentation and mathematical development that an updated AFIT RAIL RF collection system has been developed that is capable of bistatic RF collections using a single moving receiver. In order to summarise lessons learnt in this thesis and provide a starting point for future experimentation and research, this section will collate all known system limitations and pertinent interactions.

4.4.1 Oscilloscope Acquisition Memory.

- As stated in Chapter II, the total acquisition memory of the oscilloscope is 64 MSamples. Using the FastFrame$^{\text{TM}}$ feature, the number of samples for any given collection is equal to $n_{\text{samp}} = n_{\text{channels}} PTf_{\text{samp}}$, as defined in (21).

  For example, the experimental set up used for the full-length signal collections uses 2 channels (transmit trigger channel and pulse receive channel), 16 frames, 200μs frames and a sampling frequency of 10 GS/s. Thus, in the experimental configuration used for full-length signal collections, the total samples recorded are $(2)(16)(200 \times 10^{-6})(10 \times 10^{9}) = 64$ MS, which is the maximum possible. Using half-length signals, there were 32 frames recorded instead of 16 frames, thus also giving 64 MS.

- Collections were attempted when removing the transmit trigger channel to enable more received data recording, but this method was found to be unreliable as the frame capture was likely to trigger on noise rather than the return pulse approximately 50% of the time. Thus, triggering the FastFrame$^{\text{TM}}$ capture using the transmit signal connected straight to the AWG is considered essential for accurate collections.

- The FastFrame^{TM} feature enables more than two channels to be recorded per capture so extending the system further to a multistatic system is possible. However, as n_{channels} is increased, the length of available collection data on each channel is significantly reduced.

4.4.2 Waveform Generation.

- The AWG has two transmit channels available and the ability to output two waveforms simultaneously. However, the updated Matlab GUI presented here will have to be modified to enable loading separate pulses in to each channel of the AWG.

- Additionally, each FastFrame^{TM} collection can only use one channel as a trigger, despite having the ability to record more than two channels, so timing and synchronisation issues will have to be considered if extending the AWG for use with multiple signals.

4.4.3 Experimental Configuration.

- The aperture length used throughout this thesis is $D = 1.92$ m, although the track is 1.97 m in length. The slightly shorter distance was chosen in previous AFIT research [2–11] to maximise aperture length whilst still providing symmetry about the 1.0 m station for ease of geometric configuration.

- Scene configuration is a major issue in collecting repeatable experimental results. For example, a high RCS on a close target can lead to far targets being lost during the image normalisation process, as discussed in Chapter III for the outdoor experimental scene. In determining an appropriate RCS for a close target(s), calibration has to be done manually by observing the central range profile and ensuring that all target returns have similar amplitudes.

- It was mentioned that spotlight SAR processing techniques were used despite the experimental configuration actually following spotlight SAR methodology. Further investigation is needed to confirm the assumptions of beamwidth uniformity are valid.

4.4.4 Signal Processing.

- After conducting an RF collection using the updated Matlab software interface, the signal processing process used for constructing SAR images involves the following steps:

    1. Export collected pulse data from the oscilloscope and save to laptop/hard drive.
    2. Establish folder structure for given experiment and extract single pulse capture file to individual pulse records.
    3. Analyse data collect using the respective scene setup files to customise scene geometry, calibration delay, pulse position vectors and number of pulses to drop.
    4. Create separate image data for an empty scene and remove from final image if desired to remove clutter anomalies.

- The current method works well once a particular experimental folder has been established but there is potential to automate several steps currently done through trial and error, such as determining the calibration delay or ideal number of pulses to drop.

V. Conclusions and Future Work

This chapter outlines the conclusions drawn from this research and presents various areas for future work that were not achievable within the timeframe of this project. Work conducted through this thesis is summarised and final thoughts are provided for the reader.

5.1 Summary

This research set out to improve previous AFIT experimental methodology to enable moving RF collection through a simple hardware configuration and software interface. Additionally, areas for distortion in moving SAR collections were investigated with compensation techniques proposed, and simulations were presented to support theoretical and experimental findings. The process of updating methodology to enable moving collections was described in detail and experimental results show images constructed using both rudimentary and updated software interfaces.

For all experimental configurations, error analysis was conducted. It was seen that, given the look angles and receiver velocities under test, Doppler shift effects were small enough that the focus of error compensation shifted to MMEs. A robust simulation tool was developed to realistically simulate Doppler shift and MME effects and verify the theoretical results obtained. Various methods of error characterisation were conducted and analysis of expected error was conducted. Lastly, multiple approaches to MME compensation were investigated with a combination of pulse position estimation and dropping pulses at each end of the collection producing the most accurate images. Additionally, it was seen that anomalies within the final SAR images still existed and that further refinement of experimental technique was needed to create more pristine SAR images.

5.2 Future Work

Proposed future work for this project revolves around further refining the hardware capabilities of the system and expanding the variety of scenarios under test to enable investigation of more complicated radar and SAR imaging phenomena. Suggested areas of focus include:

- Further diversify experimental scene geometry to further investigate SAR phenomena and possible errors, such as adding a moving target for further Doppler shift investigation.
- Incorporate a second transmit signal into AWG (and Matlab GUI) to enable multistatic scenarios.
- Implement signal mixing on the receive signal to downconvert the frequency, thus lowering the required sampling frequency and facilitating better usage of the oscilloscope acquisition memory.
- Update the experimental laptop to enable shorter processing times, thus lowering the effects of synchronisation and algorithm processing times.
- Conduct an uncertainty analysis on experimental assumptions made in the updated AFIT RAIL SAR system, such as the use of spotlight SAR processing techniques, chosen receiver motion error values, disregarding environmental effects in outdoor testing or the accuracy of computer processing times measured.

5.3 Final Thoughts

This thesis has shown that, using current AFIT hardware, an updated experimental system has been achieved. The updated experimental system is capable of moving RF collections controllable through a customised Matlab GUI. Robust simulations were also developed throughout this research to investigate Doppler shift and MME effects. Using preliminary experimental and simulated results, error characterisation was conducted and compensation methods proposed.

Using the developed error compensation techniques, final experimental results were presented on an indoor scene to show that the updated AFIT RAIL RF collection system is capable of creating SAR images through a moving collection and reducing image distortions through various signal processing techniques. Whilst there are numerous areas available for future work, this thesis has shown promising development in the AFIT RAIL experimental system and understanding of motion related errors in SAR images.

Bibliography

1. N. Willis, *Bistatic Radar*. Raleigh, NC: SciTech Publishing, Inc., 2005.

2. A. S. Evers, "Evaluation and application of LTE, DVB, and DAB signals of opportunity for passive bistatic SAR imaging," Master's thesis, Wright State University, April 2014.

3. A. S. Evers and J. A. Jackson, "Experimental passive SAR imaging exploiting LTE, DVB, and DAB signals," in *IEEE Radar Conference*, May 2014, pp. 0680–0685.

4. ——, "Analysis of an LTE waveform for radar applications," in *IEEE Radar Conference*, May 2014, pp. 0200–0205.

5. J. Gutierrez Del Arroyo and J. Jackson, "WiMAX OFDM for passive SAR ground imaging," *IEEE Transactions on Aerospace and Electronic Systems*, vol. 49, no. 2, pp. 945–959, April 2013.

6. ——, "SAR imaging using WiMAX OFDM PHY," in *IEEE Radar Conference*, May 2011, pp. 129 –134.

7. ——, "Collecting and processing WiMAX ground returns for SAR imaging," in *IEEE Radar Conference*, 29 Apr-3 May 2013, pp. 1–6.

8. A. S. Evers and J. A. Jackson, "Cross-ambiguity characterization of communication waveform features for passive radar," *IEEE Transactions on Aerospace and Electronic Systems*, October 2015.

9. J. Gutierrez del Arroyo, "Passive synthetic aperture radar imaging using commercial OFDM communication networks," Ph.D. dissertation, Air Force Institute of Technology, Sep. 2012.

10. J. Gutierrez Del Arroyo and J. Jackson, "Range profiles from an experimental OFDM passive radar," in *International Waveform Diversity and Design Conference*, Jan. 2012.

11. J. Gutierrez del Arroyo, J. Jackson, and M. Temple, "Receive signal processing for OFDM-based radar imaging," in *IEEE International Conference on Acoustics, Speech and Signal Processing (ICASSP)*, May 2013, pp. 2775–2779.

12. F. Canini, A. Di Lallo, L. Timmoneri, and D. Vigilante, "Use of digital-television terrestrial (DTV) signals for passive radars," in *2010 11th International Radar Symposium (IRS)*, June 2010, pp. 1–4.

13. R. Saini and M. Cherniakov, "DTV signal ambiguity function analysis for radar application," *IET Proceedings of Radar, Sonar and Navigation*, vol. 152, no. 3, pp. 133–142, June 2005.

14. T. Oyedokun, "Feasibility study of DTV based PCL radar in South Africa," in *European Radar Conference (EuRAD)*, Oct 2011, pp. 186–189.

15. T. Peto, L. Dudas, R. Seller, and P. Renner, "Digital television broadcast-based passive radar research and development," in *2014 20th International Conference on Microwaves, Radar, and Wireless Communication (MIKON)*, June 2014, pp. 1–4.

16. W. Xianrong, W. Junfang, H. Sheng, and T. Hui, "Reconstruction of reference signal for DTMB-based passive radar systems," in *IEEE CIE International Conference on Radar*, vol. 1, Oct 2011, pp. 165–168.

17. D. O'Hagan and C. Baker, "Passive bistatic radar (PBR) using FM radio illuminators of opportunity," in *IEEE Workshop on New Trends for Environmental Monitoring Using Passive Systems,*, Oct 2008, pp. 1–6.

18. M. Malanowski, K. Kulpa, J. Kulpa, P. Samczynski, and J. Misiurewicz, "Analysis of detection range of fm-based passive radar," *IET Radar, Sonar & Navigation*, vol. 8, no. 2, pp. 153–159, February 2014.

19. M. Malanowski, K. Kulpa, P. Samczynski, J. Misiurewicz, and J. Kulpa, "Long range fm-based passive radar," in *IET International Conference on Radar Systems*, Oct 2012, pp. 1–4.

20. U. Mendi and B. Sarkar, "Passive radar using multiple GSM transmitting stations," in *International Radar Symposium*, May 2006, pp. 1–4.

21. P. Krysik, P. Samczynski, M. Malanowski, L. Maslikowski, and K. Kulpa, "Velocity measurement and traffic monitoring using a GSM passive radar demonstrator," *IEEE Aerospace and Electronic Systems Magazine*, vol. 27, no. 10, pp. 43–51, Oct 2012.

22. P. Krysik, M. Wielgo, J. Misiurewicz, and A. Kurowska, "Doppler-only tracking in GSM-based passive radar," in *17th International Conference on Information Fusion (FUSION)*, July 2014, pp. 1–7.

23. A. Salah, R. Abdullah, A. Ismail, F. Hashim, C. Leow, M. Roslee, and N. Rashid, "Feasibility study of LTE signal as a new illuminators of opportunity for passive radar applications," in *IEEE International RF and Microwave Conference*, Dec 2013, pp. 258–262.

24. H. Sun, D. Tan, Y. Lu, and M. Lesturgie, "Applications of passive surveillance radar system using cell phone base station illuminators," *IEEE Aerospace and Electronic Systems Magazine*, vol. 25, no. 3, pp. 10–18, March 2010.

25. A. Buonanno, M. D'Urso, and L. Palmieri, "WiFi-based passive bistatic radar by using moving target indicator and least square adaptive filtering," in *IEEE*

International Symposium on Phased Array Systems Technology, Oct 2013, pp. 174–179.

26. N. Willis and H. Griffiths, Eds., *Advances in Bistatic Radar*. Raleigh, NC: SciTech Publishing, Inc., 2007.

27. B. Rigling and R. Moses, "Motion measurement errors and autofocus in bistatic SAR," *IEEE Transactions on Image Processing*, vol. 15, no. 4, pp. 1008–1016, April 2006.

28. X. Zhong, M. Xiang, H. Yue, and H. Guo, "Algorithm on the estimation of residual motion errors in airborne SAR images," *IEEE Transactions on Geoscience and Remote Sensing*, vol. 52, no. 2, pp. 1311–1323, Feb 2014.

29. Q. Yalin, Z. Qingjun, and G. Jiajia, "Effect of satellite attitude errors on spotlight SAR image," in *IET International Radar Conference*, April 2013, pp. 1–5.

30. S. Bing, W. Ye, C. Jie, W. Yan, and L. Bing, "Image position analysis of motion errors for missile-borne SAR based on diving model," in *IEEE International Conference on Imaging Systems and Techniques*, Oct 2013, pp. 206–209.

31. Y. Shao, R. Wang, Y. K. Deng, Y. Liu, R. Chen, G. Liu, T. Balz, and O. Loffeld, "Error analysis of bistatic SAR imaging and stereoscopy bistatic SAR," *IEEE Transactions on Geoscience and Remote Sensing*, vol. 51, no. 8, pp. 4518–4543, Aug 2013.

32. D. Giudici, D. D'Aria, A. Guarnieri, A. Bazzoni, and R. Venturini, "Analysis of antenna pointing errors on SAR image quality," in *IEEE Radar Conference*, May 2008, pp. 1–6.

33. J. Lee, H.-L. Lou, D. Toumpakaris, and J. Cioffi, "Effect of carrier frequency offset on OFDM systems for multipath fading channels," in *IEEE Global Telecommunications Conference*, vol. 6, Nov 2004, pp. 3721–3725.

34. C. Jakowatz, D. Wahl, P. Eichel, D. Ghiglia, and P. Thompson, *Spotlight-Mode Synthetic Aperture Radar: A Signal Processing Approach*. Norwell, MA: Kluwer Academic Publishers, 1996.

35. European Telecommunications Standards Institute, "LTE: Evolved universal terrestrial radio access (E-UTRA), physical channels and modulation," European Telecommunications Standards Institute, Tech. Rep., April 2010. [Online]. Available: http://www.etsi.org/deliver/etsi_ts/136200_136299/136211/09.01.00_60/ts_136211v090100p.pdf

36. ——, "Digital Video Broadcasting (DVB); framing structure, channel coding and modulation for digital terrestrial television," European Telecommunications Standards Institute, Tech. Rep., January 2009. [Online]. Available: http://www.etsi.org/deliver/etsi_en/300700_300799/300744/01.06.01_60/en_300744v010601p.pdf

37. ——, "Radio broadcasting systems; Digital Audio Broadcasting (DAB) to mobile, portable and fixed receivers," European Telecommunications Standards Institute, Tech. Rep., June 2006. [Online]. Available: http://www.etsi.org/deliver/etsi_en/300400_300499/300401/01.04.01_60/en_300401v010401p.pdf

38. "AirMax sector antenna datasheet," Ubiquiti Networks Inc., 2013. [Online]. Available: https://dl.ubnt.com/datasheets/airmaxsector/airMAX_Sector_Antennas_DS.pdf

39. *TDS6000B & TDS6000C Series Digital Storage Oscilloscopes Quick Start User Manual*, Tektronix, Jan 2006.

40. J. Munson, D.C., J. O'Brien, and W. Jenkins, "A tomographic formulation of spotlight-mode synthetic aperture radar," *Proceedings of the IEEE*, vol. 71, no. 8, pp. 917–925, Aug 1983.

41. M. Zatman, "How narrow is narrowband?" *IEEE Proceedings of Radar, Sonar and Navigation*, vol. 145, no. 2, pp. 85–91, Apr 1998.

42. N. Levanon and E. Mozeson, *Radar Signals*. Hoboken, NJ: John Wiley & Sons, Inc., 2004.

43. G. Kino, *Acoustic waves: devices, imaging, and analog signal processing*, ser. Prentice-Hall Signal Processing Series. Englewood Cliffs, NJ: Prentice Hall PTR, 1987.

44. C. Oliver and S. Quegan, *Understanding Synthetic Aperture Radar Images*. Raleigh, NC: SciTech Publishing, Inc., 2004.

45. S. Taylor, G. Antonello, and S. Rogers, "OFDM frame structure," IEEE 802.16 Broadband Wireless Access Working Group, Tech. Rep., January 2011. [Online]. Available: http://www.ieee802.org/16/tga/contrib/C80216a-02_16.pdf

46. J. Jackson, B. Rigling, and R. Moses, "Canonical scattering feature models for 3D and bistatic SAR," *IEEE Transactions on Aerospace and Electronic Systems*, vol. 46, no. 2, pp. 525–541, April 2010.

47. *Universal Controller SCX10 Operating Manual*, Oriental Motor Co., Ltd., 2011.

REPORT DOCUMENTATION PAGE

Form Approved
OMB No. 0704–0188

1. REPORT DATE *(DD–MM–YYYY)*	2. REPORT TYPE	3. DATES COVERED *(From — To)*
24–03–2016	Master's Thesis	Sep 2014 — Mar 2016

4. TITLE AND SUBTITLE

Hardware Development and Error Characterisation for the AFIT RAIL SAR System

5a. CONTRACT NUMBER

5b. GRANT NUMBER

5c. PROGRAM ELEMENT NUMBER

6. AUTHOR(S)

Schmidt, Dayne A., Flight Lieutenant, RAAF

5d. PROJECT NUMBER

5e. TASK NUMBER

5f. WORK UNIT NUMBER

7. PERFORMING ORGANIZATION NAME(S) AND ADDRESS(ES)

Air Force Institute of Technology
Graduate School of Engineering and Management (AFIT/EN)
2950 Hobson Way
WPAFB OH 45433-7765

8. PERFORMING ORGANIZATION REPORT NUMBER

AFIT-ENG-MS-16-M-043

9. SPONSORING / MONITORING AGENCY NAME(S) AND ADDRESS(ES)

Sensors Directorate
2241 Avionics Circle, Bldg 600
WPAFB OH 45433-7318
COMM 937-528-8124
Email: braham.himed@us.af.mil

10. SPONSOR/MONITOR'S ACRONYM(S)

AFRL/RYMD

11. SPONSOR/MONITOR'S REPORT NUMBER(S)

12. DISTRIBUTION / AVAILABILITY STATEMENT

DISTRIBUTION STATEMENT A:
APPROVED FOR PUBLIC RELEASE; DISTRIBUTION UNLIMITED.

13. SUPPLEMENTARY NOTES

14. ABSTRACT

This research is focussed on updating the Air Force Institute of Technology (AFIT) Radar Instrumentation Lab (RAIL) Synthetic Aperture Radar (SAR) experimental system. Firstly, this research assesses current hardware limitations and updates the system configuration and methodology to enable collections from a receiver in motion. Secondly, orthogonal frequency-division multiplexing (OFDM) signals are used to form (SAR) images in multiple experimental and simulation configurations. This research analyses, characterises and attempts compensation of relevant SAR image error sources, such as Doppler shift or motion measurement errors (MMEs). Error characterisation is conducted using theoretical, simulated and experimental methods. Final experimental results are presented to verify performance of the updated SAR collection system and show improvements to the final product through an updated methodology and various signal processing techniques.

15. SUBJECT TERMS

synthetic aperture radar (SAR), hardware development, error characterisation, motion measurement errors (MME), Doppler shift

16. SECURITY CLASSIFICATION OF:			17. LIMITATION OF ABSTRACT	18. NUMBER OF PAGES	19a. NAME OF RESPONSIBLE PERSON
a. REPORT	b. ABSTRACT	c. THIS PAGE			Dr Julie Jackson,(ENG)
U	U	U	UU	106	19b. TELEPHONE NUMBER *(include area code)* (937) 255-3636 x4678; julie.jackson@afit.edu